The Role of Surface Potential Vorticity in the Vertical Structure of Mesoscale Eddies in Wind-Driven Ocean Circulations

WENDA ZHANG,[a] STEPHEN M. GRIFFIES,[a,b] ROBERT W. HALLBERG,[a,b] YI-HUNG KUO,[a] AND CHRISTOPHER L. P. WOLFE[c]

[a] *Program in Atmospheric and Oceanic Sciences, Princeton University, Princeton, New Jersey*
[b] *NOAA/Geophysical Fluid Dynamics Laboratory, Princeton, New Jersey*
[c] *School of Marine and Atmospheric Sciences, Stony Brook University, State University of New York, Stony Brook, New York*

(Manuscript received 6 October 2023, in final form 24 January 2024, accepted 4 March 2024)

ABSTRACT: The vertical structure of ocean eddies is generally surface-intensified, commonly attributed to the dominant baroclinic modes arising from the boundary conditions (BCs). Conventional BC considerations mostly focus on either flat- or rough-bottom conditions. The impact of surface buoyancy anomalies—often represented by surface potential vorticity (PV) anomalies—has not been fully explored. Here, we study the role of the surface PV in setting the vertical distribution of eddy kinetic energy (EKE) in an idealized adiabatic ocean model driven by wind stress. The simulated EKE profile in the extratropical ocean tends to peak at the surface and have an *e*-folding depth typically smaller than half of the ocean depth. This vertical structure can be reasonably represented by a single surface quasigeostrophic (SQG) mode at the energy-containing scale resulting from the large-scale PV structure. Due to isopycnal outcropping and interior PV homogenization, the surface meridional PV gradient is substantially stronger than the interior PV gradient, yielding surface-trapped baroclinically unstable modes with horizontal scales comparable to or smaller than the deformation radius. These surface-trapped eddies then grow in size both horizontally and vertically through an inverse energy cascade up to the energy-containing scale, which dominates the vertical distribution of EKE. As for smaller horizontal scales, the EKE distribution decays faster with depth. Guided by this interpretation, an SQG-based scale-aware parameterization of the EKE profile is proposed. Preliminary offline diagnosis of a high-resolution simulation shows the proposed scheme successfully reproducing the dependence of the vertical structure of EKE on the horizontal grid resolution.

KEYWORDS: Instability; Ocean circulation; Potential vorticity; Shallow-water equations; Eddies; Parameterization

1. Introduction

Ocean mesoscale eddies have horizontal scales of tens to hundreds of kilometers and account for a majority of oceanic kinetic energy (e.g., Ferrari and Wunsch 2009; Storer et al. 2022). These eddies are important for the transport and mixing of momentum, heat, salt, and carbon, as well as other biogeochemical tracers, and impact the large-scale circulation and climate (Wolfe and Cessi 2010; Marshall and Speer 2012; Griffies et al. 2015; Gnanadesikan et al. 2015). These eddies are yet to be fully resolved in climate models due to their relatively small size, and as a result, their effects must be parameterized. Observational and modeling studies have shown that the strength of mesoscale eddies tend to peak at the surface and decay with depth (Wunsch 1997; de La Lama et al. 2016), with the exception for certain mode-water or topographically trapped eddies that intensify in the interior or near the bottom (Zhang et al. 2017; Radko 2023). Parameterizations that properly account for the surface-intensified vertical structure are crucial for simulations of large-scale ocean circulations and density structures (Danabasoglu and Marshall 2007; Eden et al. 2009). This effort requires a better understanding and representation of the eddy vertical structure, which is the topic of this paper.

The vertical structure of eddy motions is often represented using vertical normal modes (Wunsch 1997; Wortham and Wunsch 2014; de La Lama et al. 2016). Traditionally, these modes—including the barotropic and baroclinic modes—are solutions to an eigenvalue problem with flat-bottom and rigid-lid boundary conditions (Gill 1982; Vallis 2017). The surface-intensified structure of ocean eddies is then decomposed as a linear combination of these eigenmodes in the vertical.

Notably, the barotropic and first baroclinic modes together can capture the bulk of midlatitude eddy structure and variability (Wunsch 1997; Zhang et al. 2013). That these two modes are dominant is consistent with geostrophic turbulence theory, which reveals that eddies emerging from baroclinic instability tend to transfer energy from higher baroclinic modes to the lower modes and then to the barotropic mode at scales comparable to the deformation radius (Salmon 1980; Smith and Vallis 2001). Due to surface-intensified stratification and bottom friction, ocean eddies are usually not fully barotropized and the first baroclinic contribution remains considerable (Fu and Flierl 1980; Smith and Vallis 2001). Although the barotropic and first baroclinic modes are useful for diagnosing the vertical structure of eddies, they are inefficient for quantitative predictions since their relative contribution to eddy energy varies substantially in space and time (Wunsch 1997).

Vertical mode structures can change significantly in the presence of bottom topography (Hallberg 1997; LaCasce 2017), leading to recent studies promoting a different set of baroclinic modes subject to zero horizontal velocity at the bottom due to

Corresponding author: Wenda Zhang, wenda.zhang@princeton.edu

DOI: 10.1175/JPO-D-23-0203.1

rough bathymetry (LaCasce 2017). The inclusion of the *rough bottom* tends to decouple the bottom pressure from the interior, yielding modified baroclinic structures that are more surface-intensified (Rhines 1970; Hallberg 1997; Samelson 1992; Tailleux and McWilliams 2001). The first baroclinic mode derived under such rough-bottom setup captures a larger fraction of observed velocity variance than the traditional first baroclinic mode (de La Lama et al. 2016; Ni et al. 2023) and has recently been used for diagnoses and parameterizations of the vertical structure of eddy velocity and mixing (Adcroft et al. 2019; Groeskamp et al. 2020; Stanley et al. 2020; Holmes et al. 2022).

Still, these rough-bottom modes assume a zero buoyancy anomaly at the ocean surface, whereas ocean eddies exhibit strong surface temperature and salinity anomalies (Lapeyre 2009; Hausmann and Czaja 2012; Frenger et al. 2015). Theoretical studies have proposed vertical-mode bases that include surface buoyancy anomalies, associating with surface-trapped responses that decay quasi-exponentially from the surface (Lapeyre and Klein 2006; Smith and Vanneste 2013; Yassin and Griffies 2022a). The surface-trapped mode is governed by the surface quasigeostrophic (SQG) dynamics in the presence of a surface horizontal buoyancy gradient (Blumen 1978; Held et al. 1995; Lapeyre and Klein 2006; Lapeyre 2017). Previous studies noted that the SQG mode can capture the surface intensification of the observed eddies better than the traditional baroclinic structures, pointing to surface buoyancy anomalies being key to establishing the vertical distribution of ocean eddies (Lapeyre and Klein 2006; Lapeyre 2009).

The SQG framework has been adapted to infer the eddy properties in the vertical from surface observations and hydrography in the midlatitude ocean in both modeling (Lapeyre and Klein 2006; Isern-Fontanet et al. 2008; Wang et al. 2013; Ponte and Klein 2013; Liu et al. 2014; Qiu et al. 2016; Fresnay et al. 2018; Qiu et al. 2020; Miracca-Lage et al. 2022) and observational studies (LaCasce and Mahadevan 2006; Rocha et al. 2013; Liu et al. 2017). Such inference, however, depends on the spectra of the surface eddy energy or buoyancy because the vertical structure of the SQG mode depends on the horizontal eddy scale—smaller eddies tend to have shallower structures (Lapeyre 2017; Ajayi et al. 2020). The scale dependence seemingly limits the application of the SQG framework to the parameterization of eddies for ocean models in which mesoscale features are not fully resolved.

Here, we argue that knowing the energy-containing scale is sufficient to determine the dominant SQG mode, supporting a sparse representation of the vertical structure of mesoscale eddies. Assuming the energy-containing scale is given and using this information in lieu of the full surface spectra, we propose an SQG-based, scale-aware parameterization for the vertical structure of ocean eddies. Focusing on the dependence of vertical structure on horizontal scales, offline analyses with output from an idealized adiabatic ocean model demonstrate that the proposed scheme reproduces the desired distributions of unresolved eddies by models with different horizontal resolutions. The only remaining step for a completely closed parameterization is the determination of the horizontal energy-containing scale, which is a topic outside the scope of this paper.

Why does the SQG mode at the energy-containing scale play such an important role in the vertical eddy structure? We propose that geostrophic turbulence theory offers insights to this question. Surface buoyancy anomalies are often represented as surface-confined potential vorticity (PV) anomalies (Bretherton 1966). The horizontal PV gradient tends to be substantial at the ocean surface, yielding surface-trapped instabilities, such as Charney and mixed-layer instabilities (Smith 2007; Fox-Kemper et al. 2008; Tulloch et al. 2011; Roullet et al. 2012; Callies et al. 2016; Schubert et al. 2020; Feng et al. 2021, 2022). The link between baroclinic instability and the vertical structure of mesoscale eddies is investigated here in an idealized adiabatic ocean model. We find that the SQG-like profile of eddy kinetic energy (EKE) is prevalent in purely wind-driven circulations analogous to those in the Atlantic Ocean. The simulated EKE exhibits (i) a surface-intensified profile consistent with the SQG mode at the energy-containing scale and (ii) a dependence of vertical distribution on the horizontal eddy scale. Although our adiabatic model does not have surface buoyancy forcing and a mixed layer, the isopycnal outcropping due to wind forcing gives rise to a strong surface meridional PV gradient. In the upper ocean, the interior PV gradient is weak due to eddy mixing, which tends to homogenize the PV within geostrophic contours (Rhines and Young 1982b). Such a large-scale PV distribution induces surface-trapped baroclinically unstable modes with an SQG-like vertical structure. These surface-trapped eddies supply energy to the energy-containing eddy through an inverse energy cascade, ultimately shaping the EKE profile.

This manuscript is organized as follows. Section 2 covers equations of the baroclinic and surface-trapped modes for theoretical background. The numerical model configuration and Wentzel–Kramers–Brillouin (WKB) solutions for the SQG mode are given in section 3. In section 4, we reveal the key role of SQG modes in setting the vertical structure of EKE, which can be determined by the horizontal energy-containing scale. In section 5, we argue that the dominance of the SQG mode arises from baroclinic instability and the corresponding inverse energy cascade, which are surface-trapped due to the upper-ocean PV structures. Based on these understandings, in section 6, we propose a SQG-based parameterization for the subgrid EKE profile that depends on the numerical model horizontal grid spacing. The results are summarized, and their implications for understanding the eddy vertical structure are discussed in section 7.

2. Theoretical background

In this section, we recap elements from QG theory, focusing on (i) the vertical structure of baroclinic modes and (ii) modifications to take into account a surface buoyancy anomaly.

a. Baroclinic modes

The vertical structure of ocean eddies is commonly represented using vertical normal modes of the linearized QG

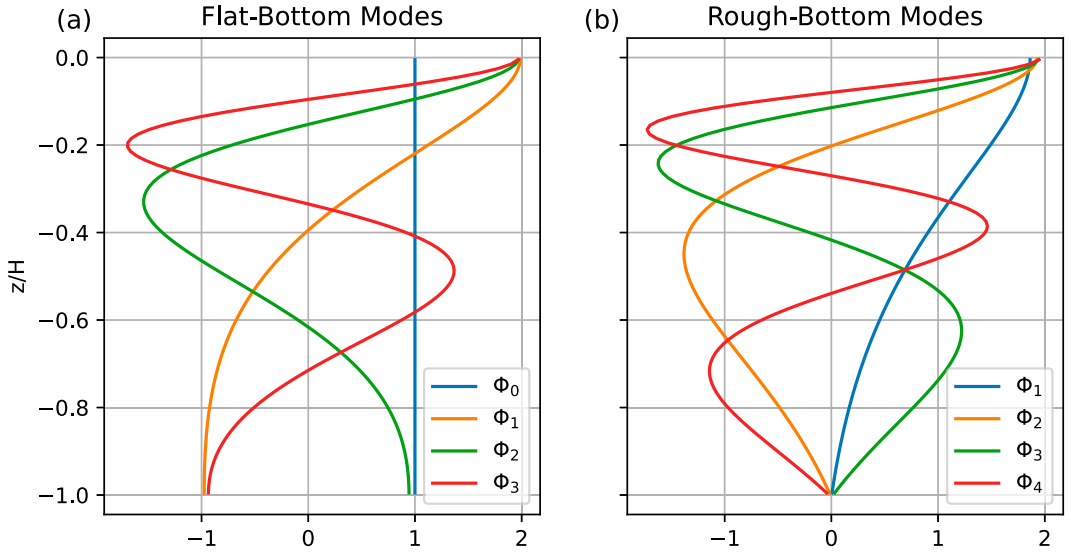

FIG. 1. The first four vertical normal modes solved from the eigenvalue problem in Eq. (3) with (a) flat-bottom and rigid lid boundaries and (b) rough-bottom and rigid-lid boundaries. The stratification decays exponentially with depth following an *e*-folding scale of a third of the water depth in both cases. Each profile of Φ_m is normalized so that $\int_{-H}^{0} \Phi_m^2 dz/H = 1$. Blue, orange, green, and red lines indicate the first, second, third, and fourth modes. The first mode Φ_0 in (a) is depth independent and called the barotropic mode, while the other modes are baroclinic (BC) modes. The Φ_0 mode in (b) is represented by bottom-trapped topographic waves, which are not plotted here. The first mode Φ_1 in (b) is often called the EBT mode.

equations for a quiescent ocean state (e.g., chapter 6 of Vallis 2017),

$$\frac{\partial}{\partial t}\left[\nabla^2\psi + \frac{\partial}{\partial z}\left(\frac{f^2}{N^2}\frac{\partial \psi}{\partial z}\right)\right] + \beta\frac{\partial \psi}{\partial x} = 0, \tag{1}$$

where $\psi(x, y, z, t)$ is the streamfunction perturbation, f is the Coriolis parameter, β is the meridional derivative of f, and $N^2 = \partial B/\partial z$ is the squared buoyancy frequency defined via the large-scale buoyancy B. Note that ψ and $\partial\psi/\partial z$ are proportional to the pressure and buoyancy anomalies, respectively.

Substituting the wave-like ansatz

$$\psi = \hat{\psi}_0 \Phi(z) \exp[i(k_x x + k_y y - \omega t)] \tag{2}$$

into Eq. (1) yields an eigenvalue problem for the nondimensional vertical structure function Φ:

$$\frac{d}{dz}\left(\frac{f^2}{N^2}\frac{d\Phi}{dz}\right) = -\lambda^2\Phi. \tag{3}$$

Here, $\hat{\psi}_0$ is proportional to the 2D Fourier transform of ψ at the surface, k_x and k_y are the zonal and meridional wavenumbers, respectively, ω is the angular frequency, and λ^2 is the reciprocal of squared deformation radius.

Solving Eq. (3) requires surface and bottom boundary conditions (BCs). It is common to assume the flat-bottom and rigid-lid conditions in which the buoyancy vanishes:

$$\frac{d\Phi}{dz} = 0 \text{ at } z = 0, -H. \tag{4}$$

Equations (3) and (4) constitute a Sturm–Liouville problem for Φ, admitting a set of orthogonal normal modes $\{\Phi_m\}$, with the corresponding eigenvalues $\{\lambda_m^2\}$. Here, the integer, $m \geq 0$, counts the number of zeros of $\Phi_m(z)$ in the interior. The solution with $m = 0$ denotes the barotropic mode, and the infinity of $m \geq 1$ solutions are the baroclinic modes. The first few modes are shown in Fig. 1a as computed with an exponential stratification profile whose *e*-folding scale is a third of water depth. General solutions of an eddy feature satisfying Eq. (1) and the same BCs (4) can be uniquely represented as a linear combination of these modes. See Rocha et al. (2016) for a comprehensive summary regarding the representation in terms of a predetermined basis.

An alternative structural consideration includes the bottom topography (Rhines 1970; Hallberg 1997) with which the horizontal velocity vanishes at the bottom, yielding

$$\frac{d\Phi}{dz} = 0 \text{ at } z = 0 \quad \text{and} \quad \Phi = 0 \text{ at } z = -H. \tag{5}$$

That is, the bottom BC is now imposed on the pressure anomaly, whereas the surface BC remains applied to the buoyancy anomaly. These alternative BCs result in a different set of normal modes shown in Fig. 1b, referred to as the *rough-bottom* modes or "surface modes" in LaCasce (2017) since the bottom horizontal flow is at rest. Notably, there is no longer a depth-independent barotropic mode among these—an important distinction from

the flat-bottom modes in Fig. 1a. The barotropic mode is replaced by bottom-trapped topographic waves (e.g., Rhines 1970; LaCasce 2017; Yassin and Griffies 2022a) not illustrated here. The lowest rough-bottom mode ($m = 1$; blue line in Fig. 1b)—because it does not change sign in the interior—is often referred as the equivalent barotropic (EBT) mode (Killworth 1992; Hallberg 1997; Adcroft et al. 2019). The EBT mode has been adapted for the parameterization of the vertical distribution of mesoscale eddy diffusivity, e.g., in the 0.5° version of the GFDL ocean climate model OM4.0 (Adcroft et al. 2019).

A notable feature of the two Sturm–Liouville problems considered thus far is that the horizontal wavenumbers do not appear in them, except for the bottom topographic waves that are not shown. Therefore, the vertical structure of the normal modes does not depend on the horizontal scales. This property can be attributed to the surface boundary conditions not including buoyancy anomalies (i.e., $d\Phi/dz = 0$ at $z = 0$)—an assumption shared by both of the flat- and rough-bottom setups.

b. Surface-trapped modes

To incorporate surface buoyancy anomalies, a surface-aware formulation is proposed to include the horizontal buoyancy gradient at the surface (and bottom), as briefly outlined here following Smith and Vanneste (2013) as well as Yassin and Griffies (2022a).

In this modified approach, the eigenvalue problem consists of the same differential equation [Eq. (3)] but with a set of more general BCs

$$\begin{aligned} \frac{f^2}{N^2 H}\frac{d\Phi}{dz} &= \alpha(0)(k^2 + \lambda^2)\Phi, \quad \text{at } z = 0, \\ \frac{f^2}{N^2 H}\frac{d\Phi}{dz} &= -\alpha(-H)(k^2 + \lambda^2)\Phi, \quad \text{at } z = -H, \end{aligned} \tag{6}$$

with a nondimensional function

$$\alpha(z) \equiv \frac{f}{N^2 \beta k_x}\left(k_x \frac{\partial B}{\partial y} - k_y \frac{\partial B}{\partial x}\right), \tag{7}$$

$k = (k_x^2 + k_y^2)^{1/2}$, and B is the large-scale buoyancy. The resulting eigenvalue problem differs from the standard Sturm–Liouville problem in that the wavenumbers k, k_x, and k_y, and eigenvalue λ^2 are now part of the BCs. Following Smith and Vanneste (2013), an oceanic special case is the limit where $\alpha(-H) \to 0$ (i.e., the buoyancy anomaly vanishes at the bottom) and $\alpha(0) \to \infty$ (strong horizontal buoyancy gradient and/or weak vertical stratification at the surface). The full set of normal modes in this special case consists of a surface-trapped mode, $\Phi_s(z; k)$, satisfying

$$\begin{aligned} \frac{d}{dz}\left(\frac{f^2}{N^2}\frac{d\Phi_s}{dz}\right) &= k^2 \Phi_s, \\ \Phi_s|_{z=0} &= 1, \\ \left.\frac{d\Phi_s}{dz}\right|_{z=-H} &= 0, \end{aligned} \tag{8}$$

plus the interior modes $\Phi_m(z)$ (for integer index $m \geq 1$)

$$\begin{aligned} \frac{d}{dz}\left(\frac{f^2}{N^2}\frac{d\Phi_m}{dz}\right) &= -\lambda_m^2 \Phi_m, \\ \Phi_m|_{z=0} &= 0, \\ \left.\frac{d\Phi_m}{dz}\right|_{z=-H} &= 0. \end{aligned} \tag{9}$$

The surface boundary condition, $\Phi_s|_{z=0} = 1$, in Eq. (8) is set following $\Phi|_{z=0} = 1$ [Φ is normalized by its surface value in Eq. (2)], and $\Phi_m|_{z=0} = 0$ as derived in Eq. (9). The surface BCs indicate that the surface pressure anomaly is dominated by the surface-trapped mode Φ_s. A few examples of these modes are illustrated in Fig. 2. Together, the admissible Φ_s and Φ_m form an orthogonal basis.

Note the similarity between Eq. (9) and the earlier rough-bottom setup (the surface and bottom BCs are switched here). Additionally, the vertical structure of the interior modes does not depend on horizontal scales (see Fig. 2b).

In contrast, Eq. (8) explicitly includes the horizontal wavenumber, yielding an outstanding feature of the surface-trapped mode: Larger eddies (with smaller horizontal wavenumber k) are associated with deeper modes whose vertical response decays slower with depth (see Fig. 2a). Because Φ_s has a zero interior PV anomaly and is driven by a surface buoyancy anomaly—consistent with the SQG dynamics (Blumen 1978; Held et al. 1995)—it is also referred to as the "SQG mode." The SQG mode is relevant to the oceanic cases where a horizontal buoyancy gradient intensifies near the surface (Smith 2007; Capet et al. 2016), and this mode is central to this paper.

The decomposition given by Eqs. (8) and (9) is consistent with the surface mode in Smith and Vanneste (2013) [their Eq. (19)] and is different from that proposed by Lapeyre and Klein (2006). Lapeyre and Klein (2006) use a Neumann surface boundary condition (i.e., surface buoyancy anomaly is specified) for the surface-trapped mode, while Φ_s here has a Dirichlet surface boundary condition (i.e., surface pressure anomaly is specified). Studies have found that the SQG mode using the surface pressure anomaly is better for reproducing the vertical structure of EKE than that using the surface buoyancy anomaly (Isern-Fontanet et al. 2008; Qiu et al. 2016, 2020). More details are provided in appendix A.

Both of the surface-trapped and interior modes described above assume a flat-bottom condition, i.e., vanishing bottom buoyancy anomaly; recall the bottom BCs in Eqs. (8) and (9). These are the limiting cases of Eq. (6) through which more complicated topographic effects can be included (LaCasce 2017; Yassin and Griffies 2022a) and will be explored in future work.

3. Methods

a. Model configuration

The numerical model used in this study is an idealized configuration of the Modular Ocean Model, version 6 (MOM6). This configuration is named "NeverWorld2" by Marques et al. (2022) and has been used to study mesoscale eddy parameterizations (e.g., Loose et al. 2022; Yankovsky et al. 2022). The model domain is a single basin with two hemispheres using

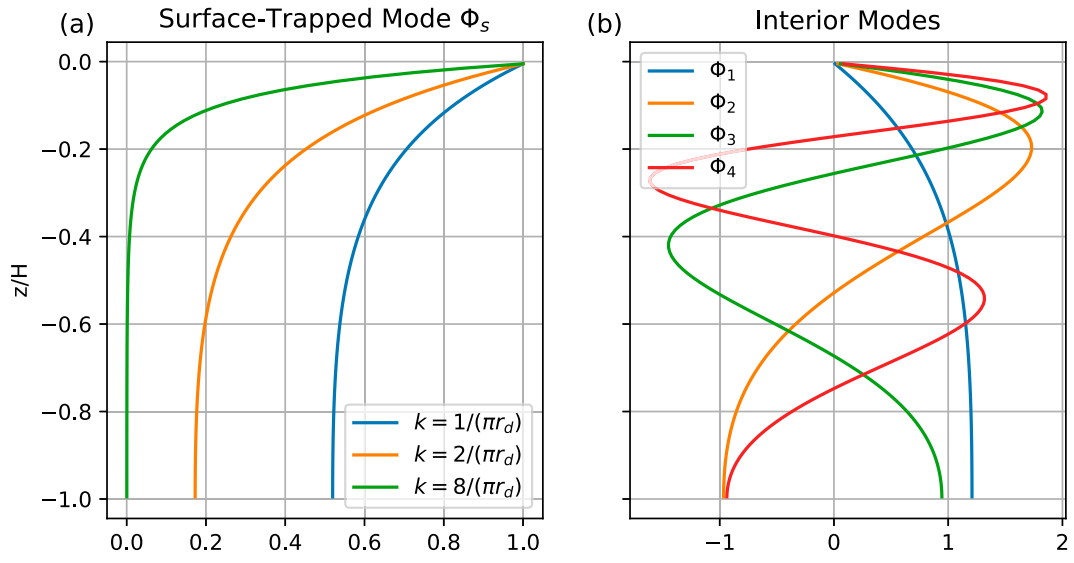

FIG. 2. Vertical profiles of the (a) surface-trapped mode (i.e., the SQG mode) and (b) interior modes, determined by solving Eqs. (8) and (9), respectively. The stratification profile is an exponential function of z, as in Fig. 1. The surface mode is calculated for three different horizontal wavenumbers, $1/(\pi r_d)$, $2/(\pi r_d)$, and $8/(\pi r_d)$, where r_d is the Rossby deformation radius of the first flat-bottom baroclinic mode (orange line in Fig. 1a). Each surface-trapped mode profile is normalized by its surface value. The lines in (b) indicate the first four interior modes, each of which is normalized in the same way as the modes in Fig. 1.

spherical coordinates. The domain extends from 70°S to 70°N in the meridional direction, 0°–60°E in the zonal direction, and has a maximum depth of 4000 m. The domain is bounded by a 200-m continental shelf along all side boundaries, except for a zonally reentrant channel located at 60°–40°S, mimicking the Southern Ocean. A ridge topography orienting meridionally spans the entire meridional extent of the domain. The ridge has a width of 40° and maximum height of 2000 m. There is a semicircular ridge with a radius of 10° spanning 0°–10°E longitude and 60°–40°S latitude that mimics the Scotia Arc across the Drake Passage.

The Boussinesq and hydrostatic primitive equations are discretized vertically using isopycnal coordinates, with a total of 15 isopycnal layers with finer spacing near the surface in the initial setup. The horizontal grid spacing is 1/32°. The model is driven solely via mechanical forcing from a zonally uniform zonal wind stress that varies meridionally and is fixed in time. There is no surface buoyancy forcing, no diabatic mixing, nor is there a mixed layer parameterization (i.e., it is a wind-driven adiabatic stacked shallow-water model). Dissipation arises from a background kinematic vertical viscosity ($A_v = 1.0 \times 10^{-4}$ m^2 s^{-1}), a dimensionless bottom drag ($C_d = 0.003$), and the horizontal friction is given by a biharmonic Smagorinsky viscosity (Griffies and Hallberg 2000). More details about the model setup and spinup are given in Marques et al. (2022).

Figure 3a shows a snapshot of the surface specific kinetic energy (KE). The black lines correspond to the 500-day mean sea surface height (SSH) contours, representing the streamlines of surface geostrophic currents outside the tropics. The circulation pattern is a caricature of the Atlantic Ocean, with subtropical gyres and western boundary currents in both hemispheres. In the Northern Hemisphere, there is a subpolar gyre, while in the Southern Hemisphere, a circumpolar current prevails in the reentrant channel. The KE illustrates the prevalence of mesoscale eddies throughout the domain. The Rossby deformation radius is resolved over most regions of the model, with the exception being the continental shelf and very high latitudes near the boundaries (Yankovsky et al. 2022).

b. Solution for the SQG mode

The SQG mode Φ_s, described by Eq. (8), is diagnosed in the stacked shallow-water model introduced above. In this model, the dynamical impact of surface buoyancy is represented by the surface-layer PV, as described by the layered QG dynamics detailed in appendixes B and D.

The SQG mode can be determined numerically for realistic stratification profiles. We can also derive an analytical solution using the WKB approximation. To get an analytical form, we assume $\Phi_s \to 0$ as $z \to -\infty$. For each horizontal wavenumber k, the WKB solution Φ_s^{WKB} is given to first order by

$$\Phi_s^{\mathrm{WKB}} = e^{kz_s}, \tag{10}$$

where

$$z_s = -\int_z^0 \frac{N}{|f|} dz, \tag{11}$$

is the stretched vertical coordinate with $z < 0$ and $z_s < 0$ in the ocean interior.

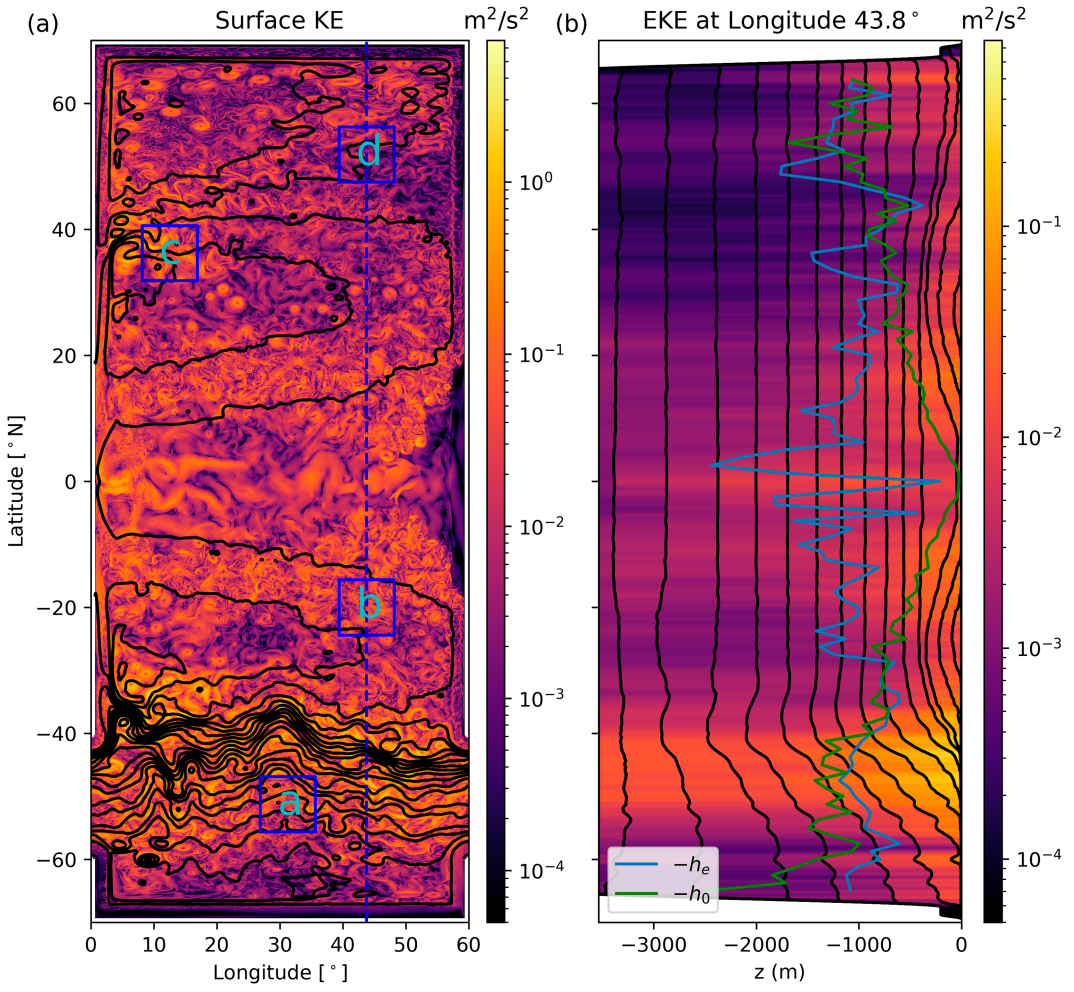

FIG. 3. (a) Snapshot of horizontal KE at the surface. Black lines are contours of the 500-day mean SSH. Blue boxes labeled a, b, c, and d indicate the 8.7° × 8.7° regions where the vertical structure of eddies is analyzed in later figures. (b) A meridional section of the EKE per unit mass along the longitude shown by the blue dashed line in (a). Black lines show all the isopycnals in the model. Blue lines indicate the e-folding depth h_e of the rms eddy velocity (square root of EKE). The green line is the deformation depth h_0 of the energy-containing scale, introduced in section 4b.

The Fourier transform of the streamfunction field associated with the SQG mode $\hat{\psi}_s$ is

$$\hat{\psi}_s^{\mathrm{WKB}} = \hat{\psi}_0 e^{kz_s}, \tag{12}$$

where $\hat{\psi}_0$ is the same as that in Eq. (2), which is the Fourier transform of the streamfunction at the surface.

Equation (10) reveals the important characteristics of the SQG mode, namely, its exponential decay with z_s and its dependence on the horizontal scale of eddies. Smaller eddies with larger wavenumber k decay faster with depth than larger eddies with smaller wavenumber. The scale dependence of the SQG mode provides valuable insights for parameterizing the vertical structure of eddies, as we discuss in section 6.

Note that Eq. (10) differs from the widely used "eSQG" method in ocean studies (Lapeyre and Klein 2006). The eSQG method assumes a constant N with depth, determined empirically to account for the impact of an internal PV gradient (Lapeyre and Klein 2006). In contrast, our formula accounts for the vertical variation of N within the stretched vertical coordinate z_s, allowing for a more accurate representation of the SQG mode itself. For example, Φ_s^{WKB} decays faster with depth in the thermocline since N is larger there. See also Yassin and Griffies (2022b) for more on SQG theory with vertically varying stratification.

4. Vertical structure of EKE

We analyze the vertical structure of EKE, defined as

$$\mathrm{EKE} = \frac{1}{2}(\overline{u'^2} + \overline{v'^2}), \tag{13}$$

where the bar ($\bar{\ }$) indicates a 500-day time mean, and the prime ($'$) is the anomaly relative to the mean and is saved in snapshots in 5-day intervals. Figure 3b shows the EKE along a meridional section indicated by the blue dashed line in

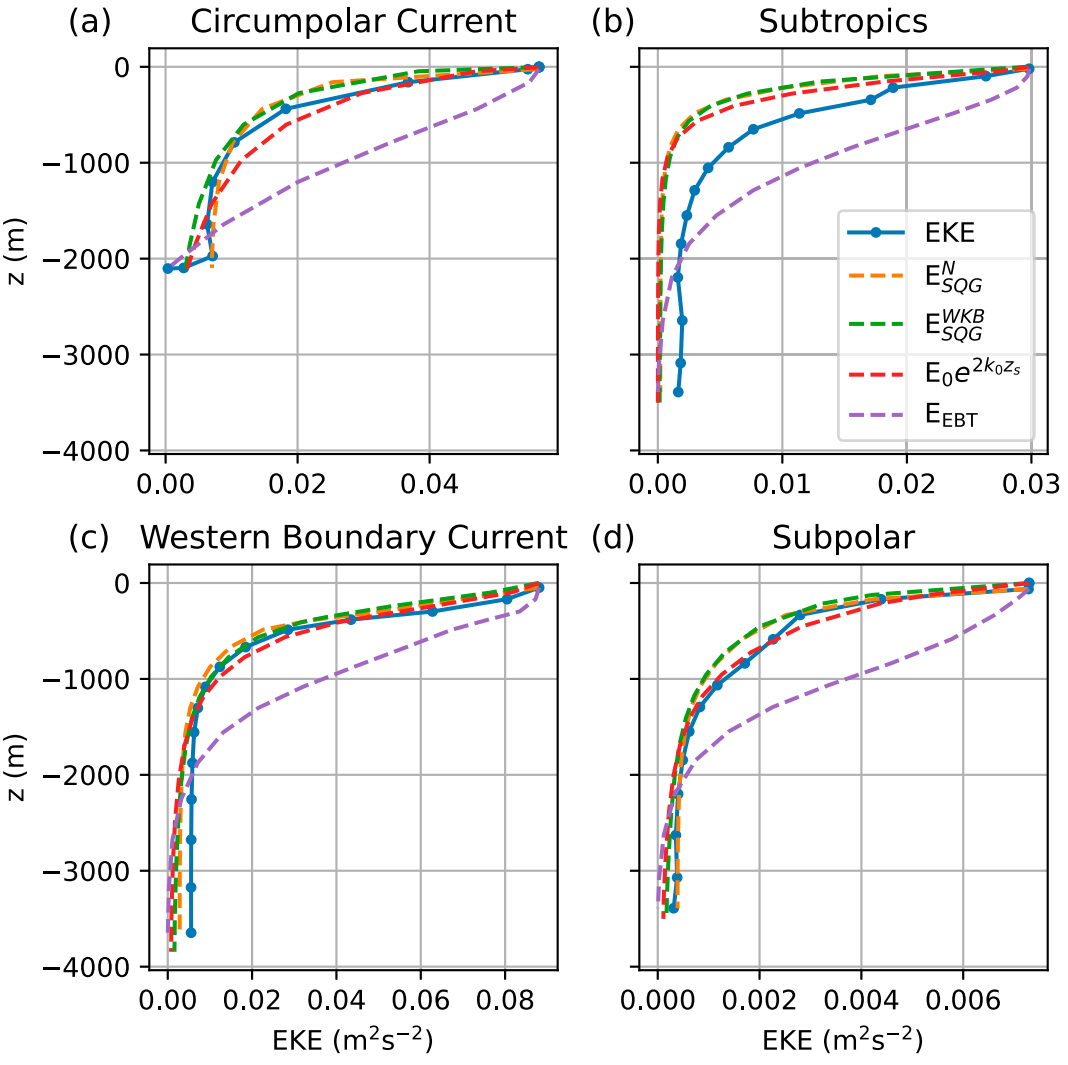

FIG. 4. Vertical profiles of the horizontally averaged EKE (solid blue lines with dots) in the four labeled regions in Fig. 3. The four regions are located in the (a) circumpolar current, (b) subtropical gyre, (c) western boundary current, and (d) subpolar regions. Dashed orange and green lines are the numerical [Eq. (8)] and WKB [Eq. (15)] solutions of the SQG mode, respectively, summed over horizontal wavenumbers of the surface EKE spectrum. Red dashed line is the WKB solution of the SQG mode at the energy-containing scale [Eq. (17)]. The purple dashed line is the vertical structure of the EBT mode.

Fig. 3a. The EKE tends to be surface-intensified. It maximizes at the surface and rapidly decays with depth in the gyre and low latitudes, while it remains significant in the deep ocean in the circumpolar current. To examine the detailed vertical structure, we select four distinct dynamical regimes, highlighted by the four blue boxes in Fig. 3a, that are located in the circumpolar current, subtropical gyre, western boundary current extension, and subpolar gyre. By examining the vertical profile of EKE in these different regions, we aim to identify the dynamics that controls the eddy vertical structure.

a. Comparison to the vertical modes

Vertical profiles of EKE in the four selected regions are shown in Fig. 4. The EKE decays rapidly with depth in the upper ocean and gradually approaches a constant in the deep ocean. The barotropic component (i.e., the depth-independent flat-bottom mode) accounts for about 78% of the total EKE in the circumpolar current region and about 50% in the other three regions.

The vertical structure of EKE is compared to the structure predicted by the EBT mode (section 2a),

$$E_{\mathrm{EBT}} = E_0 \Phi_{\mathrm{EBT}}^2, \tag{14}$$

where E_0 is the surface EKE. The square is taken because Φ_{EBT} describes the vertical structure of eddy velocity [see Eq. (2)].

The profile of E_{EBT} is shown by the purple dashed line in Fig. 4. The EBT mode is surface-intensified, but it decays

more slowly with depth than the diagnosed EKE. Furthermore, the EBT mode has a zero vertical gradient at the surface due to its boundary condition in Eq. (5), whereas the EKE has a strong vertical gradient near the surface. Another limitation is that the magnitude of the EBT mode is zero at the bottom, but the EKE can be significant at the bottom even with strong gradients in the bottom topography.

The vertical gradient of eddy velocity near the surface indicates that the surface-layer PV plays an important role in the vertical structure of EKE, thus motivating us to compare the vertical structure of EKE to the SQG mode. The WKB solution of the SQG mode, Eq. (10), gives the vertical structure of the SQG mode at each wavenumber. If we know the surface streamfunction spectrum $\hat{\psi}_0$, the vertical structure of EKE reproduced by the SQG mode, $E_{\mathrm{SQG}}^{\mathrm{WKB}}$, is

$$E_{\mathrm{SQG}}^{\mathrm{WKB}} = \frac{1}{2}\sum_k k^2 \left|\hat{\psi}_s^{\mathrm{WKB}}\right|^2 = \frac{1}{2}\sum_k k^2 |\hat{\psi}_0|^2 e^{2kz_s}. \tag{15}$$

The green dashed lines in Fig. 4 show the WKB solution of the SQG mode, $E_{\mathrm{SQG}}^{\mathrm{WKB}}$, where $\hat{\psi}_0 = g\hat{\eta}/f$ is estimated from Fourier transform of the SSH field η within the four regions indicated by the blue boxes in Fig. 3a. To check the accuracy of the WKB solution, we also compute the numerical solution of $\hat{\Phi}_s$ according to Eq. (15). The numerical solution of SQG EKE, E_{SQG}^{N}, is plotted as the orange dashed line, which is close to the WKB solution. The SQG mode captures the near exponential decay of EKE well in all the regions, with the exception of the subtropics, where EKE decays slower than the SQG mode (though faster than the EBT mode). The discrepancy in the subtropics indicates a nonnegligible role of interior modes [Eq. (9)]. Overall, the SQG mode matches the vertical structure of EKE better than the EBT mode. This finding suggests that the surface PV plays an important role in setting the vertical structure of EKE. This result is consistent with previous studies showing how the eddy vertical structure can be reconstructed by the SQG mode in realistic ocean simulations (Klein et al. 2009; Isern-Fontanet et al. 2008; Qiu et al. 2016, 2020).

b. *Relating to the energy-containing scale*

Reconstruction of the vertical structure based on the SQG mode, Eq. (15), requires knowledge of the surface energy spectrum, $k^2|\hat{\psi}_0|^2$, which is unavailable in coarse-resolution simulations. The surface energy spectrum is usually dominated by a peak, which indicates the energy-containing scale (surface energy spectra in the four regions are shown in Fig. 5). This feature suggests that the eddy vertical structure may also be dominated by the energy-containing eddy. The energy-containing wavenumber k_0 can be estimated following Thompson and Young (2006) and Zhang and Wolfe (2022),

$$k_0 = \sqrt{\frac{\overline{\langle|\nabla\eta'|^2\rangle}}{\overline{\langle\eta'^2\rangle}}}, \tag{16}$$

where η' is the spatial SSH anomaly and $\langle\,\rangle$ indicates a spatial average over each of the four box regions in Fig. 3.

The k_0 estimated by Eq. (16) is shown by the black dashed line in Fig. 5. This estimate is generally close to the peak of the energy spectrum. We then estimate the SQG mode structure at the energy-containing scale,

$$E_{\mathrm{SQG}}^{k_0} = E_0 e^{2k_0 z_s}, \tag{17}$$

which can be calculated at each grid point without Fourier analysis.

The vertical structure given by Eq. (17) is shown by the red dashed line in Fig. 4. It works similarly well as the SQG solution based on the full energy spectrum, meaning that the vertical structure of EKE can be represented by the SQG mode structure at the energy-containing scale.

Equation (17) also indicates a relation between the horizontal and vertical scales of EKE. Here, we measure the vertical scale of EKE as the e-folding depth h_e of the rms eddy velocity (i.e., $\sqrt{\mathrm{EKE}}|_{z=-h_e} = \sqrt{\mathrm{EKE}}|_{z=0}/e$). From Eq. (17), we can also estimate the e-folding depth of the SQG mode at the energy-containing scale h_0 determined by $z_s = k_0^{-1}$,

$$\int_{-h_0}^{0} \frac{N}{|f|}\,dz = k_0^{-1}, \tag{18}$$

which is also called the deformation depth of wavenumber k_0 (Pierrehumbert and Swanson 1995). If N is constant with depth, then $h_0 = k_0^{-1}|f|/N$; if not, which is the case in our model, it is solved numerically from Eq. (18). If Eq. (17) is a good approximation of the EKE vertical structure, then h_0 should be equal to h_e.

The e-folding depth h_e and the deformation depth of the energy-containing scale h_0 are compared in the meridional section in Fig. 3b. They compare well to each other in the extratropical regions (poleward of 20°), which is consistent with the good comparison between the EKE vertical structure and the SQG mode in these regions in Fig. 4. In the tropics, h_0 decreases to zero toward the equator due to the decreasing magnitude of Coriolis parameter $|f|$ in Eq. (18), while h_e remains around 1000–2000 m. The large fluctuations of h_e in the tropics might be due to the spatial variability of strong undercurrent and equatorial waves.

The comparison between h_e and h_0 at other meridional sections is similar to that in Fig. 3b. The e-folding depth h_e for the eddy velocity is generally shallower than a half of the water depth. The SQG mode captures the vertical structure of EKE well in the extratropical regions, while it is shallower than the EKE profile in the tropics. Figure 3a shows that the kinetic energy pattern is wave-like in the tropics, indicating that EKE is dominated by linear waves there, while in the extratropics, the flow field contains abundant coherent vortices, indicating the dominance of nonlinear eddies. Previous studies have shown that the eddy flux is dominated by linear waves and nonlinear eddies in the tropics and midlatitude ocean, respectively, leading to different scalings of eddy mixing in these regions (Klocker and Abernathey 2014; Zhang and Wolfe 2022). We expect that Eq. (17) is effective in describing the vertical structure of EKE for nonlinear eddies,

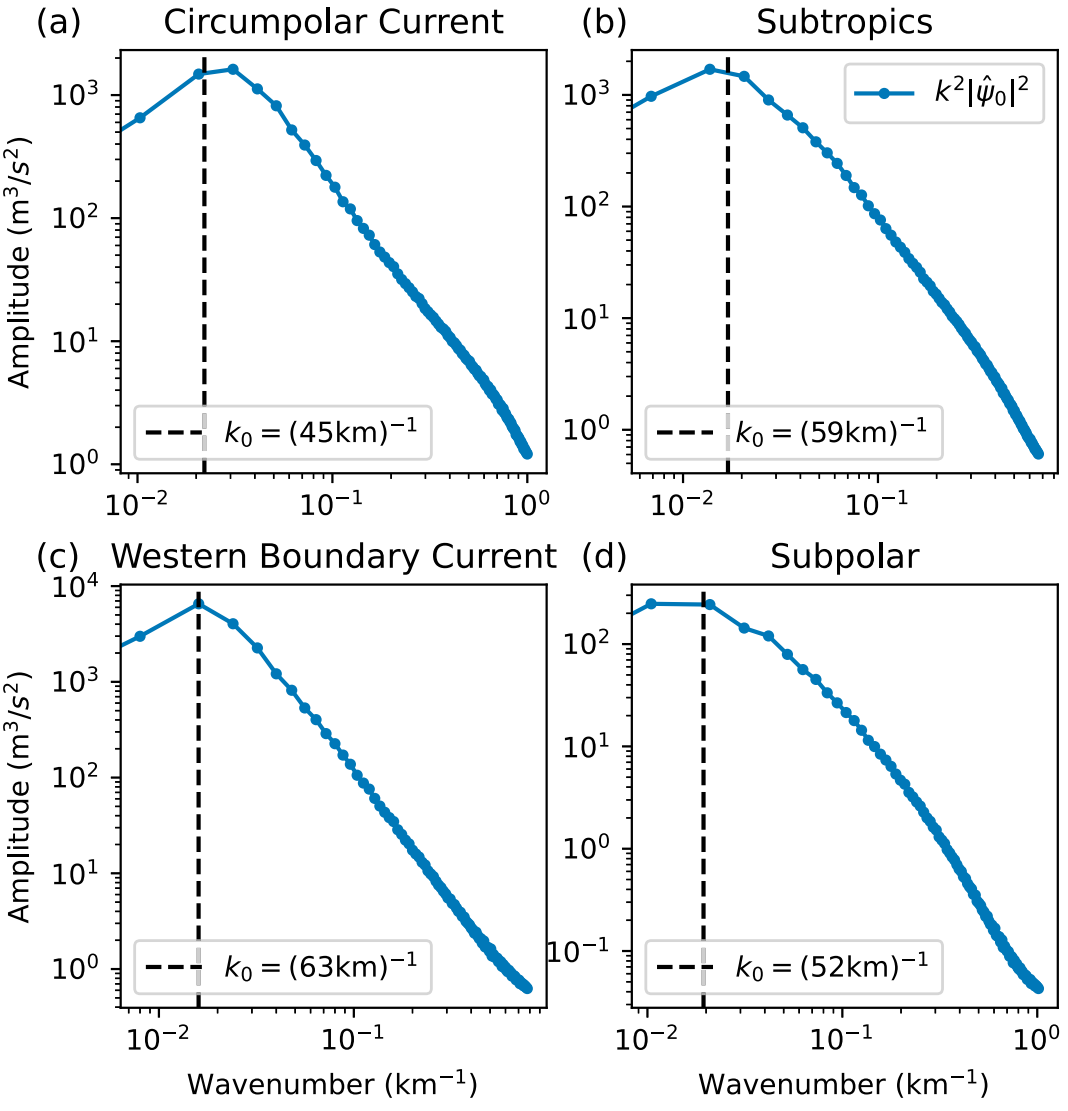

FIG. 5. (a)–(d) 1D surface KE spectrum (blue lines with dots) in the four regions shown in Fig. 3. The spectrum, $|\hat{u}|^2 + |\hat{v}|^2$, is calculated by Fourier transforming the 2D instantaneous velocity fields in 8.7° × 8.7° windows and then time averaged over 500 days. The 2D spectrum is then azimuthally integrated to obtain the 1D spectrum. The black dashed line indicates the energy-containing wavenumber k_0 estimated from Eq. (16) in the four regions. Note the log scale on both axes.

which are dominant in the extratropical ocean (Chelton et al. 2011).

5. Why is the vertical structure SQG-like?

In section 4, we have seen that the EKE structure tends to be SQG-like. Here, we discuss the underlying physics by showing (i) the EKE profile is consistent with the distributions of the eddy PV and large-scale meridional PV gradient; (ii) the surface meridional PV gradient yields baroclinic instability that produces surface-trapped unstable modes; and (iii) the kinetic energy created by baroclinic instability cascades upscale in the form of a surface-trapped mode, resulting in an SQG-like EKE profile dominated by the energy-containing eddy.

a. PV structure

SQG prescribes a zero interior PV anomaly. To examine this assumption, the rms eddy PV, q_{rms}, is computed as

$$q_{\text{rms}} = \sqrt{\overline{q'^2}}, \tag{19}$$

where q is the QG PV, estimated by Eq. (B1) in appendix B. Figure 6a shows the distribution of the rms eddy PV at the same meridional section as Fig. 3b. The eddy PV peaks at the surface layer and becomes about an order of magnitude smaller in the interior layers, which is consistent with the SQG-like EKE structure in the midlatitudes. In the subtropics (10°–25°N and 10°–25°S), the PV also intensifies

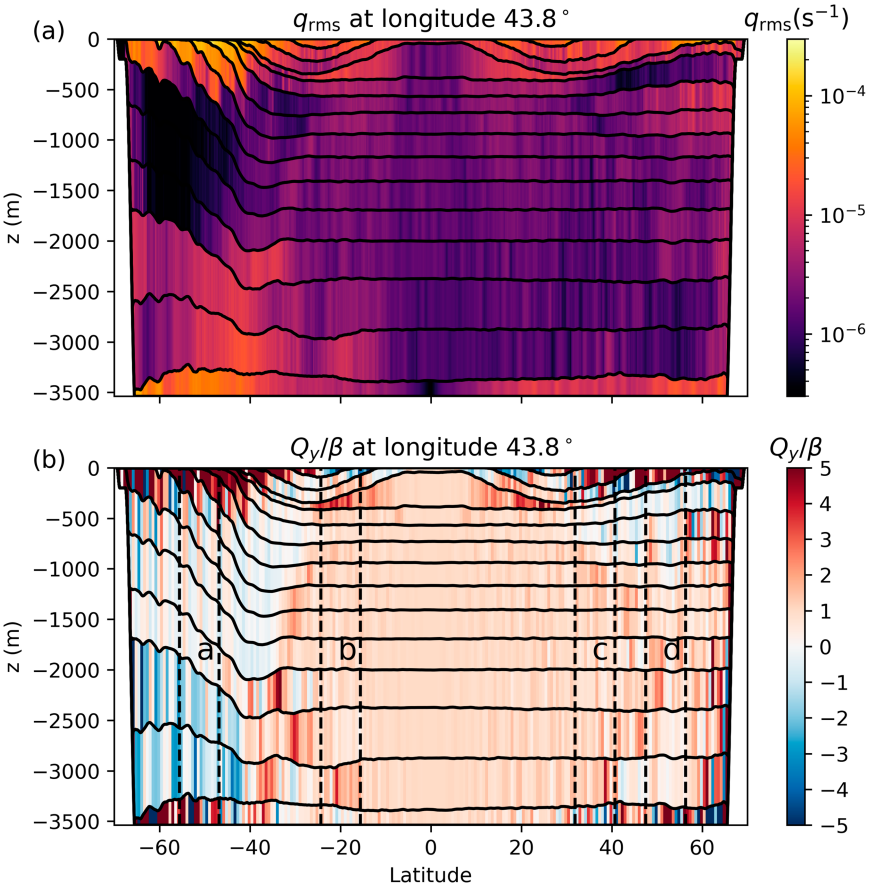

FIG. 6. Meridional and vertical distributions of (a) the rms eddy PV and (b) the meridional PV gradient normalized by β at the longitude indicated by the blue dashed line in Fig. 3a. Black solid lines are the isopycnals in the model. Black dashed lines with characters a, b, c, and d indicate the latitude range of the four regions shown in Fig. 3. Note that a and c are not in the same longitude as this meridional section.

at about 400 m, which might be why the EKE structure is less SQG-like in these regions.

The distribution of eddy PV is associated with the large-scale meridional PV gradient Q_y structure, shown in Fig. 6b. The meridional PV gradient is estimated from Eq. (C3) in appendix C for the layered shallow-water model. The magnitude of meridional PV gradient peaks at the surface due to the isopycnal outcropping. The interior PV gradient is weak compared with the surface PV gradient, especially in the upper 1000 m in the mid- and high latitudes (poleward of 30°). The weak interior PV gradient is likely due to the isopycnal mixing by eddies, which act to homogenize the PV within closed geostrophic contours in the interior (Rhines and Young 1982a,b). The large-scale PV structure shown in Fig. 6b is consistent with observations of upper-ocean circulations (Keffer 1985; Talley 1988; Pedlosky 1996). The presence of such a large-scale PV structure is responsible for the surface-intensified eddy PV distribution in Fig. 6a.

Besides the surface intensification, the magnitude of the PV gradient also intensifies in the near-bottom layers in the circumpolar current, which is consistent with the distribution of eddy PV in this region. In the subtropics, the PV gradient also peaks at about 400 m due to the flattening of isopycnals at the interior pycnocline. This pronounced interior PV gradient is likely the cause of the strong subsurface eddy PV and the deviation of the EKE profile from SQG in the low latitudes. Quantitative analyses of the impact of the PV gradient on the eddy vertical structure are given in the next section.

In addition to the variation of magnitude, the meridional PV gradient also tends to change sign from surface to the interior. In the mid- and high latitudes (except for the circumpolar current), the meridional PV gradient is positive at the surface layer, negative at layers below the surface, and positive again in the deep ocean. In the circumpolar current, the PV gradient is positive at the surface, remains weak in the interior, and becomes negative in the deep ocean. A similar distribution of the meridional PV gradient is found by Tulloch et al. (2011) (their Fig. 2a) based on oceanic reanalysis climatology. Tulloch et al. (2011) also reveals a positive surface PV gradient in the subtropics, a feature that is missing in our simulation. Figure 6b shows that the surface PV gradient is negative in the subtropics due to the upward isopycnal slope

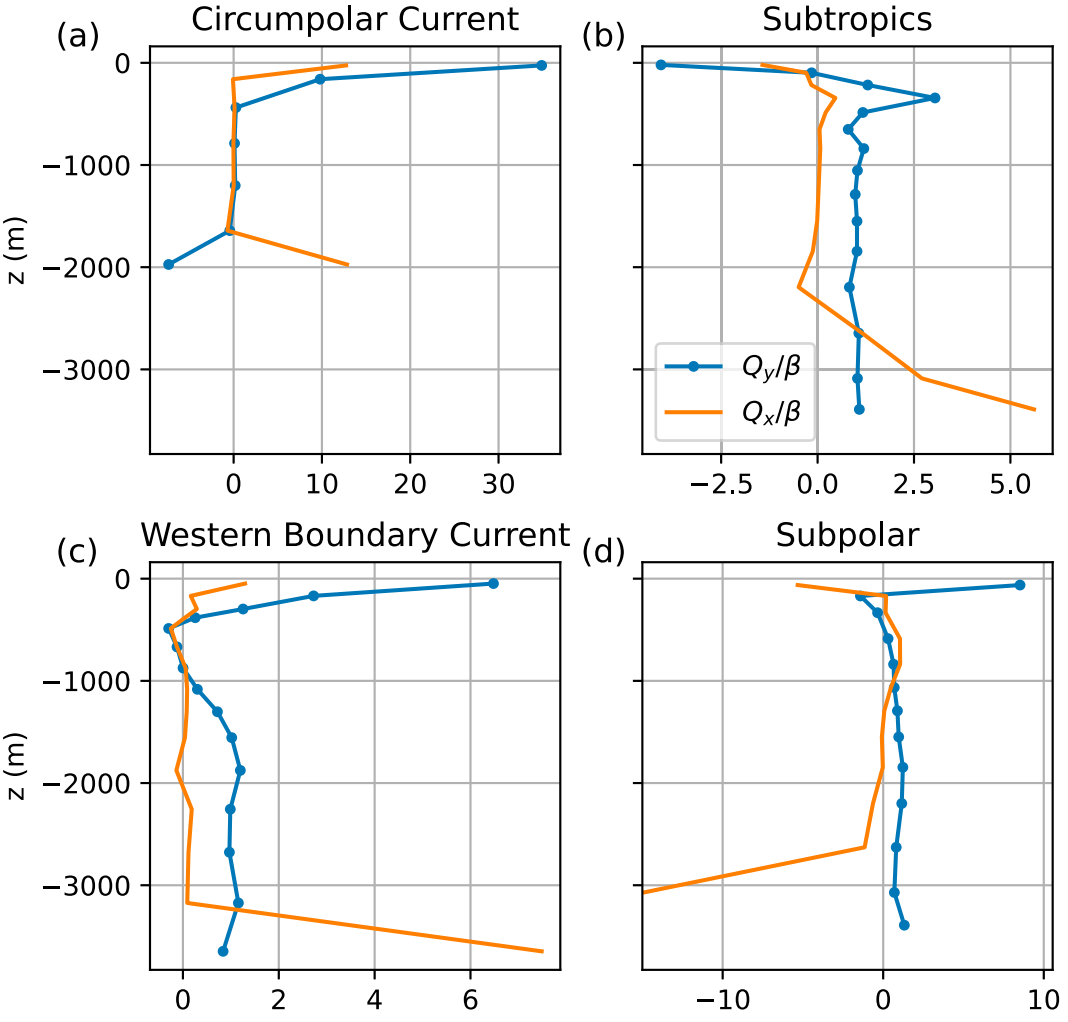

FIG. 7. (a)–(d) Vertical profiles of meridional (blue lines with dots at the layer centers) and zonal (orange lines) PV gradient normalized by β in the four regions shown in Fig. 3.

toward the equator, while in the real ocean, surface buoyancy forcing can generate a negative surface buoyancy gradient (equivalent to a positive surface PV gradient) by reversing the near-surface isopycnal slope in the subtropics. Since the NeverWorld2 model is forced by wind stress only, this positive surface PV gradient is not captured by the simulation.

b. *Linear stability*

The meridional PV gradient is often found to play a crucial role in oceanic baroclinic instability, which is an important energy source for mesoscale eddies (Smith 2007; Tulloch et al. 2011; Capet et al. 2016). A necessary condition for baroclinic instability is for the background horizontal PV gradient to change sign in the vertical, which is a typical feature of the meridional PV gradient shown in Fig. 6b.

We analyze baroclinic stability in the four regions discussed in section 4. The vertical profiles of the meridional and zonal PV gradients in the four regions are shown in Fig. 7. Figure 8 shows the distribution of the growth rate σ of unstable modes, which are solved from the eigenvalue problem described by Eq. (C6) in appendix C. Figure 9 shows the vertical structure of the most unstable mode, indicated by the cyan point in Fig. 8. The orange dashed line indicates the SQG mode at the same horizontal wavenumber as the unstable mode. We compare the vertical structure of the most unstable mode with the SQG mode and connect this result to the interpretation of the EKE profile in these four regions.

In the circumpolar current, the interior PV gradients are about ten times smaller than the surface and bottom gradients. The surface and bottom meridional PV gradients are opposite to each other, which gives rise to unstable modes at scales larger than the deformation radius. The vertical structure of the most unstable mode intensifies at both surface and bottom, which is a typical feature of the Eady-type instability arising from the interaction between the surface and bottom edge waves (Eady 1949). The Eady unstable mode is also observed in the Southern Ocean (Tulloch et al. 2011; Feng et al. 2021). The unstable mode is similar to the SQG mode in the

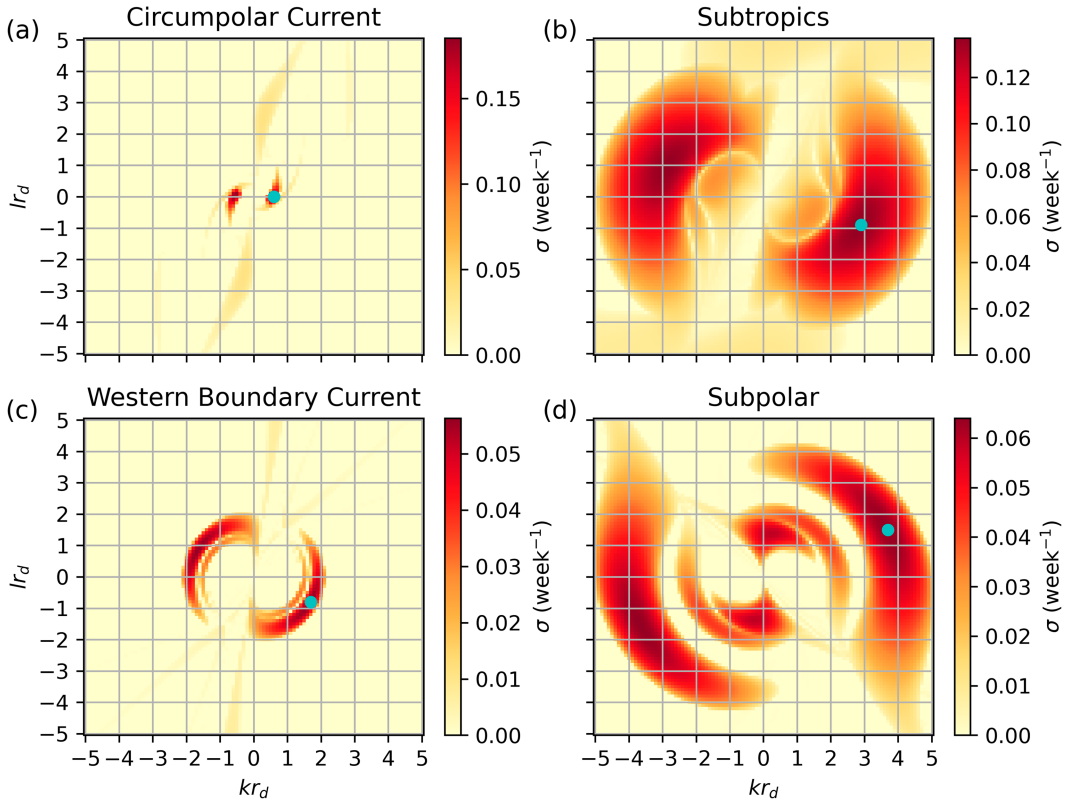

FIG. 8. (a)–(d) Growth rate of unstable modes as a function of zonal and meridional wavenumbers, k_x and k_y, respectively, that are normalized by the deformation radius in the same four regions as in Fig. 3. The cyan point indicates the most unstable mode.

upper ocean but not in the deep ocean because of the bottom intensification of the unstable mode. Conversely, the vertical structure of EKE only shows a slight intensification near the bottom and appears more like the SQG mode than the unstable mode in this region (Fig. 4a). The difference between the unstable mode and EKE is likely due to the strong damping by friction at the bottom, thereby reducing the bottom intensification of EKE.

In the western boundary current and subpolar regions, both the meridional and zonal PV gradient changes sign near the surface. The meridional PV gradient is generally stronger than the zonal gradient, except near the bottom, where the zonal PV gradient is large due to the ridge topography. The most unstable mode occurs at scales smaller than the deformation radius in these two regions. The vertical structure of the most unstable mode is surface-intensified, indicating a Charney-type instability arising from the interaction between surface edge waves and interior Rossby waves (Charney 1947). These unstable mode structures are consistent with those observed in the Gulf Stream and North Pacific regions (Tulloch et al. 2011; Capet et al. 2016). The vertical structure of the unstable mode resembles the SQG mode, similar to the vertical structure of EKE in the two regions (Figs. 4c,d).

Although the meridional PV gradient also changes sign at 500–1000-m depth, nearly all unstable modes are surface-intensified in the western boundary current and subpolar regions (not shown), indicating that the instability is always associated with surface edge waves. The Rossby wave propagates eastward in the negative PV gradient layers and westward in the positive PV gradient layers below (the zonal mean flow is eastward above 1000 m and becomes weak below), so they cannot couple to each other due to the mismatch between their zonal phase speeds. Consequently, the sign change of meridional PV gradient at 500–1000 m does not lead to the Phillips type instability (Phillips 1954) in the interior. For the same reason, the zonal PV gradient also does not induce Phillips instability in the deep ocean, although the bottom zonal PV gradient is strong due to the topography.

In the subtropics, the meridional PV gradient is negative at the top layer (note that the real ocean has a positive surface PV gradient above the top layer here) and positive in the interior. Such a PV gradient profile induces Charney-type instability—the growth rate of the unstable mode maximizes at scales smaller than the deformation radius, and the vertical structure of the most unstable mode is surface-intensified. This unstable mode structure is similar to that observed in the subtropical Atlantic Ocean (Tulloch et al. 2009), despite the absence of a positive surface PV gradient in the subtropics in our simulation. The unstable mode also exhibits a subsurface maximum, which deviates from the SQG mode. This subsurface intensification is likely attributed to the intensified meridional PV gradient at around 400 m due to the rapid vertical variation of isopycnal

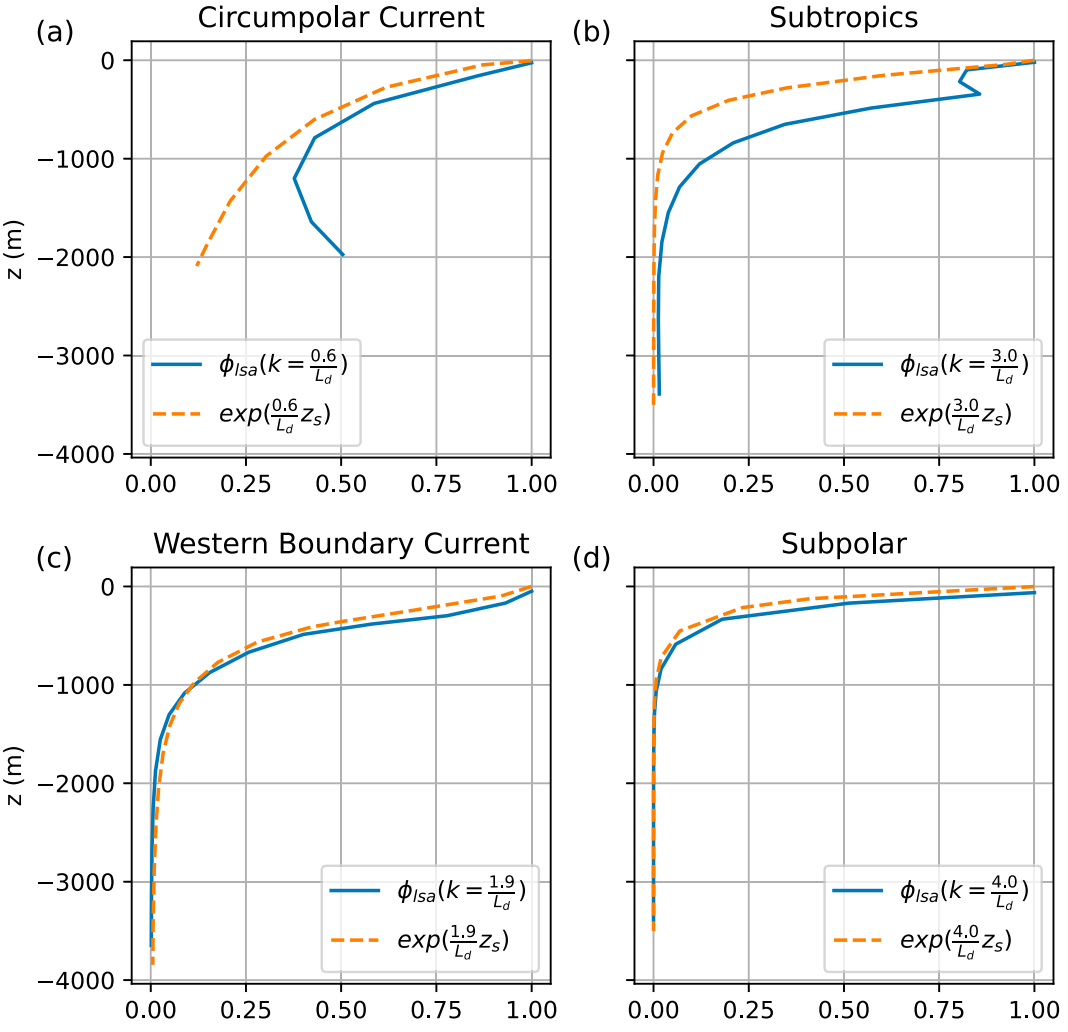

FIG. 9. (a)–(d) Vertical structure of the most unstable mode (blue solid line) indicated by the cyan point in Fig. 8. The orange dashed line is the normalized vertical structure of the SQG mode at the same wavenumber as the unstable mode.

slope at the pycnocline in this region (Figs. 6b and 7b). Such subsurface intensification of unstable modes might contribute to the deviation of the vertical structure of EKE from the SQG mode in this region (Fig. 4b).

Lapeyre (2009) also notes that the SQG mode contributes a minor fraction to the velocity variance in the subtropical Atlantic Ocean based on a realistic simulation. This suboptimal performance of the SQG mode is attributed to the negative correlation between interior and surface meridional PV gradients near the surface, a pattern akin to the observation that meridional PV gradient changes sign near the surface in the subtropics in our model (Fig. 7b). In the western boundary current and subpolar regions, the meridional PV gradient also changes sign in the upper ocean, consistent with Lapeyre (2009)'s Fig. 12a where the regression of PV on surface buoyancy is negative at 200–500 m in the Gulf Stream and North Atlantic Current. We attribute the good performance of the SQG mode in these two regions to the significantly weaker negative PV gradient in the upper ocean compared to the positive surface PV gradient (Figs. 7c,d).

The resemblance between the unstable modes and the SQG mode is attributed to the large-scale PV structure, shown in Fig. 6b, manifesting as a much stronger surface meridional PV gradient than an interior PV gradient. Although the large-scale circulations are purely wind-driven in our shallow-water model, a similar PV structure has been observed in the ocean (Talley 1988; Tulloch et al. 2011). As a result, the Charney- and Eady-type instabilities have been found to be prevalent in the midlatitude ocean (Capet et al. 2016; Feng et al. 2021), consistent with the results of our simulation. Phillips-like instability, characterized by subsurface-intensified unstable mode structures, has also been observed in the subtropical and midlatitude ocean, particularly during the summer (Feng et al. 2022). The relatively rare occurrence of such subsurface-intensified instability in our model may be attributed to the absence of surface buoyancy forcing. Such forcing is known to

enhance the near surface stratification during the summer, reducing the prevalence of Charney instability (Capet et al. 2016). The cases discussed here are thus more relevant to ocean situations during the winter and spring.

The surface PV gradient also plays an important role in the mixed layer instability, which is not present in our model due to its lack of a mixed layer. Eddies generated by mixed layer instability exhibit characteristics similar to the Eady mode within the mixed layer and resemble SQG modes below the base of the mixed layer (Callies et al. 2016). Mixed layer instability is thus analogous to the Charney instability in its ability to generate surface-trapped unstable modes, with the distinction that the "surface" for the former shifts to the base of the mixed layer.

c. Role of the energy cascade

Linear stability analysis does not account for the energy cascade arising from nonlinear interactions. We here diagnose the kinetic energy budget to identify the role of nonlinear advection in the eddy vertical structure. The layerwise KE equation is

$$\frac{\partial \mathrm{KE}_n}{\partial t} = -\mathbf{u}_n \cdot (\mathbf{u}_n \cdot \nabla \mathbf{u}_n) - \mathbf{u}_n \cdot \nabla M_n + \mathbf{u}_n \cdot \mathbf{F}_n, \tag{20}$$

where M_n is the Montgomery potential and $\mathbf{F}_n$ contains the wind stress and bottom friction, as well as vertical and horizontal viscous friction.

The first term on the RHS of Eq. (20) is the KE tendency due to nonlinear advection, which is not accounted for in the linear stability analysis. The role of nonlinear advection is examined by decomposing it in spectral space. The cospectrum of the nonlinear advection T_n is calculated as

$$T_n = -\mathrm{Re}\left[\overline{\hat{\mathbf{u}}_n^{\,*} \cdot \widehat{(\mathbf{u}_n \cdot \nabla \mathbf{u}_n)}}\right], \tag{21}$$

where $\mathrm{Re}(\cdot)$ indicates taking the real part, $(\cdot)^*$ is the complex conjugate, and $\overline{\cdot}$ indicates a 500-day average.

The advection term T_n quantifies the spectral tendency of KE due to the KE cascade between horizontal wavenumbers. The positive and negative values of $T_n(k)$ indicate that energy cascade deposits and removes KE, respectively, for eddies at the corresponding wavenumber k. The time tendency term on the LHS of Eq. (20) is close to zero when taking a long-time average. In this case, the energy cascade balances the net energy source or sink due to the work by the horizontal pressure gradient [second term on the RHS of Eq. (20)], forcing and dissipation [third term on the RHS of Eq. (20)] at each wavenumber. The work by the horizontal pressure gradient includes the contribution from the divergence of 3D energy transport by pressure and the conversion of potential energy (PE) to KE due to baroclinic instability (Capet et al. 2008).

Figure 10 shows the distribution of T_n at horizontal wavenumber and depth in the four regions. The vertical structure of T_n is generally surface-intensified and decays faster with depth at smaller scales (larger wavenumbers), which is consistent with characteristics of the SQG mode. In the circumpolar current, the energy cascade removes energy at around the deformation radius. This energy sink due to the energy cascade intensifies at both the surface and bottom, which is consistent with the unstable mode of the Eady instability at this region (section 5b), indicating that the energy cascade balances the baroclinic instability at these wavenumbers. At the other three regions, the energy cascade mainly removes energy from scales smaller than the deformation radius. This energy sink concentrates near the surface, which is likely to balance the energy source due to the Charney baroclinic instability in these regions. There is also an energy sink at small wavenumbers at around 1000 m in the subtropical and subpolar regions, though it is about an order of magnitude smaller than the value of T_n at the surface. This sink is likely to balance the baroclinic instability at small wavenumbers in these two regions (see the growth rate distribution in Fig. 8).

The energy cascade deposits energy at scales larger than the deformation radius in all the four regions (red color in Fig. 10). This energy source due to energy cascade maximizes at the energy-containing scale (purple dashed line in Fig. 10), where it is balanced by energy conversion from KE to PE and friction (not shown). The vertical distribution of the energy source remains surface-trapped at the energy-containing scale, giving rise to the SQG-like EKE profile there.

The energy cycle shown in Fig. 10 is illustrated by the schematic in Fig. 11, which is motivated by a similar schematic in Roullet et al. (2012). The forcing inputs PE to circulation at the large scales. The PE is converted to KE at scales that are close to or smaller than the deformation radius through baroclinic instability. The baroclinic instability is generally dominated by the surface PV gradient, which gives rise to surface-trapped unstable modes. These unstable modes cascade KE from small scales to large scales through their nonlinear interactions until the cascade is halted at the energy-containing scale. Consequently, the vertical structure of EKE is dominated by the mode structure at the energy-containing scale, which is deeper than the original unstable modes but still remains surface-trapped.

6. A scale-aware parameterization

Section 4 shows that SQG modes play an important role in setting the vertical structure of EKE. How can this finding inform a parameterization of the eddy vertical structure? A crucial property of the SQG mode is the coupling of its vertical and horizontal scales. As shown by the analytical expression (10), smaller horizontal scale eddies, which have a larger horizontal wavenumber, decay more rapidly with depth than larger eddies. In the context of eddy parameterization, the focus is on representing the subgrid EKE that is unresolved by the model. As the model grid spacing is refined, the scale of unresolved eddies becomes smaller, resulting in a shallower vertical structure of subgrid EKE. This result suggests that parameterization of the vertical structure of subgrid EKE should depend explicitly on the model grid spacing.

To examine the scale dependence of the eddy vertical structure, we employ high-pass spatial filters on the eddy velocity fields to compare the vertical structure at different horizontal scales. Figure 12 shows the normalized vertical structures for

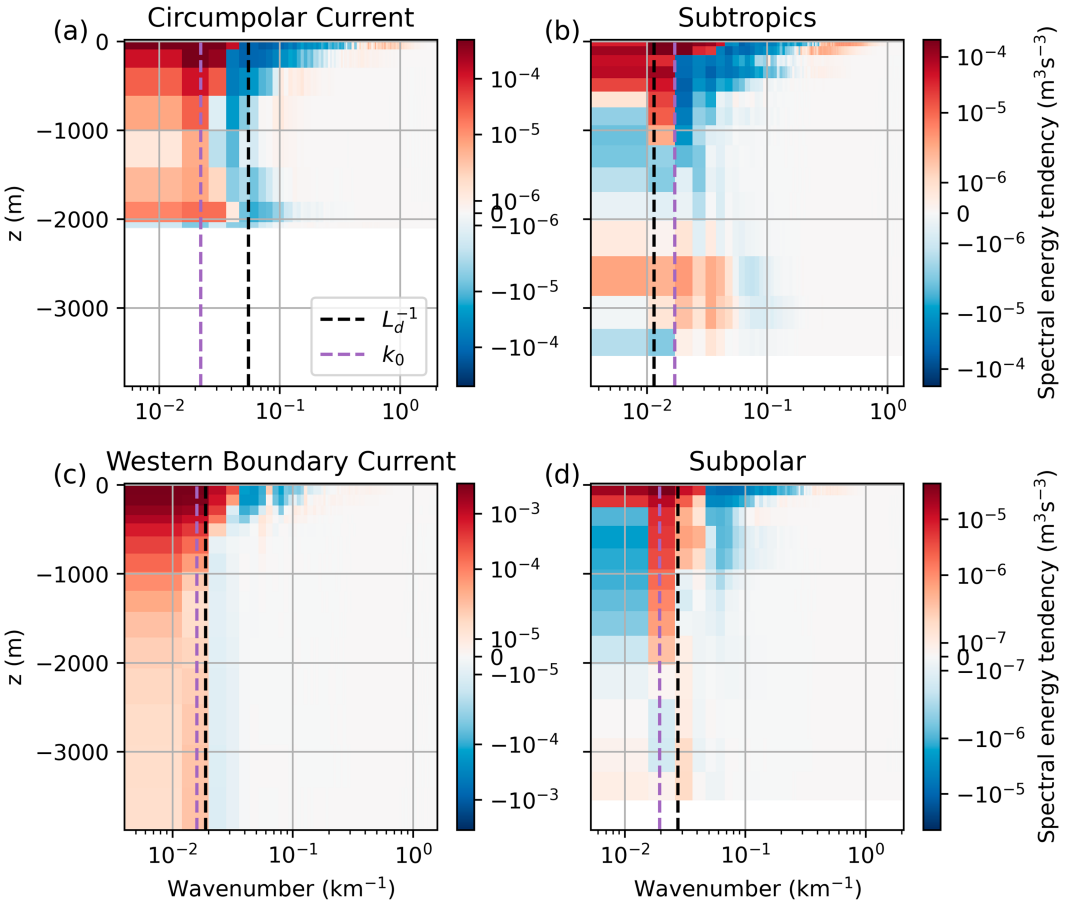

FIG. 10. Cospectrum of the advection term of KE, T_n, as a function of horizontal wavenumber and depth in the four regions shown in Fig. 3. Blue color indicates that nonlinear advection removes KE from the corresponding wavenumber, which balances the KE source by other terms on the RHS of the KE equation [Eq. (20)], while red color means that nonlinear advection supplies KE to balance the KE sink by the other terms. The black dashed line indicates the inverse of the Rossby deformation radius. The purple dashed line indicates the energy-containing wavenumber k_0. Note the different color range for each panel.

eddies smaller than $2\pi/0.25°$, $2\pi/0.5°$, and $2\pi/1°$, represented by the solid blue, orange, and green lines, respectively. The vertical structure of EKE becomes shallower as the horizontal scale becomes smaller. This finding is consistent with the prediction by SQG, highlighting the scale dependence of the eddy vertical structure.

To represent the scale-dependent eddy vertical structure at different model resolutions, we propose a scale-aware parameterization of the normalized EKE profile E_p:

$$E_p = e^{2k_g z_s}, \tag{22}$$

with

$$k_g = \max(k_0, c/\Delta), \tag{23}$$

where Δ is the model grid spacing and c is a dimensionless constant, which will be a tuning parameter. The ratio c/Δ is proportional to the largest wavenumber resolved by the model with grid spacing Δ. The constant c is on the order of 1 and determined by the minimum number of grid points needed to resolve a wavelength ($c = 1$ means that the model needs about 6 grid points to resolve a wavelength since $2\pi/6\Delta \approx 1/\Delta$). If $k_0 > c/\Delta$, the energy-containing scale is unresolved by the model, so the vertical structure of the subgrid EKE is dominated by the energy-containing wavenumber k_0. If $k_0 < c/\Delta$, the energy-containing scale is resolved, so the vertical structure of subgrid EKE will be dominated by the largest resolved wavenumber (i.e., c/Δ).

To evaluate the effectiveness of the parameterization [Eq. (22)], we conduct tests by varying Δ to 0.25°, 0.5°, and 1° and assume $c = 1$, which means that we assume a minimum of 6 grid points is required to resolve an eddy. Figure 12 shows that the parameterization profiles, estimated by Eq. (22), look similar to the vertical structure of subgrid EKE in 0.25°, 0.5°, and 1° model grid spacings, with the exception for the subtropics where the parameterization tends to decay faster than the subgrid EKE. This

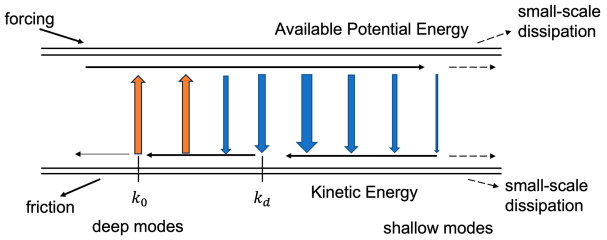

FIG. 11. Energy schematic modified from Roullet et al. (2012). The forcing supplies available PE (upper horizontal lines). The available PE cascades to smaller scales and is then converted to KE (lower horizontal lines) through baroclinic instability (blue arrows) at a broad range of horizontal scales that are close to or smaller than the deformation radius, $1/k_d$. The unstable modes arising from the instability are surface-trapped, which decay faster with depth at smaller scales. The KE of these unstable modes cascades from small scales (shallow modes) to large scales (deep modes) until the cascade is halted at the energy-containing scale, $1/k_0$. Part of the KE is dissipated by the friction, and the remainder is converted back to available PE (orange arrows) at around the energy-containing scale.

result is consistent with the comparison between the SQG mode and the total EKE in Fig. 4.

The parameterization based on Eq. (22) requires a prediction of the energy-containing scale. Studies have estimated the energy-containing scale as the Rossby deformation radius (Stone 1972), width of the baroclinic zone (Visbeck et al. 1997), Eady length scale (Larichev and Held 1995; Jansen et al. 2015), and Rhines scale (Jansen et al. 2015, 2019). Examination of these theories for predicting the eddy scale is beyond the scope of this study and will be pursued in the forthcoming work.

7. Discussion and conclusions

This study addresses the question of why ocean mesoscale eddies are surface-intensified—at least those realized within our adiabatic and wind-driven shallow-water model—with an aim to parameterize the vertical structure of mesoscale eddies. Unlike previous studies that explain the eddy vertical structure from the perspective of baroclinic modes (Wunsch 1997; de La Lama et al. 2016; LaCasce 2017; Brink and Pedlosky 2020; Quan et al. 2023), we attribute the eddy vertical structure to the baroclinic instability and the energy cascade. The vertical structure of EKE is found to be well-represented by a single SQG mode of the energy-containing scale in the extratropics, indicating that the surface PV plays a dominant role in the vertical structure of mesoscale eddies.

a. Baroclinic instability and the surface-trapped mode

The prevalence of the SQG mode is attributed to the surface-trapped baroclinic instability and energy cascade. Although the model used in this study does not have surface buoyancy forcing, the wind forcing induces isopycnal outcropping, leading to pronounced surface meridional PV gradients. The interior PV gradient is much weaker compared with the surface PV gradient due to the interior PV homogenization by eddies. Linear stability analysis shows that the surface PV gradient plays a dominant role in baroclinic instability, giving rise to surface-trapped unstable modes. These unstable modes are often smaller than the Rossby deformation radius, except in the circumpolar current where they are close to the deformation radius. Through nonlinear interactions, unstable modes transfer their kinetic energy upscale to energize mesoscale eddies, which have an energy-containing scale larger than the deformation radius but retain the surface-trapped vertical structure.

Early geostrophic turbulence theory shows that baroclinic eddies tend to transfer their energy to the barotropic (depth independent) mode, and then barotropic eddies cascade their energy upscale (Charney 1971; Salmon 1980). Later studies have found that ocean eddies are not fully barotropic, and as a consequence, the inverse energy cascade can occur in both the barotropic and baroclinic modes (Smith and Vallis 2001; Scott and Arbic 2007). In this study, we propose a different interpretation of the eddy energy cycle. Instead of decomposing the energy into the barotropic and baroclinic modes, we find that the energy cascade can directly occur among surface-trapped modes. The vertical and horizontal scales of these surface-trapped modes are coupled—smaller eddies decay faster with depth. Consequently, as eddies transfer energy to larger horizontal scales, they also grow deeper, in alignment with the barotropization tendency of geostrophic turbulence (Charney 1971; Salmon 1980). Although eddies can become nearly barotropic if their horizontal scales are an order of magnitude larger than the deformation radius, the inverse energy cascade tends to be halted at a scale that is comparable to the deformation radius. As a result, the vertical structure of energy-containing eddies is surface-intensified, similar to the SQG mode.

b. Parameterization of vertical structure based on SQG

The vertical structure of EKE depends on the horizontal scale, with smaller eddies decaying faster with depth. This feature suggests that the parameterization of eddy vertical structure should account for the horizontal scale of unresolved eddies. As the model grid spacing becomes finer, the unresolved eddies will be smaller and have a shallower vertical structure. Based on the WKB solution of the SQG mode, we propose a scale-aware parameterization of the vertical structure of EKE [Eqs. (22) and (23)]. This parameterization requires the specification of an eddy horizontal scale that depends on the model grid spacing. If the energy-containing scale is not resolved, the vertical structure parameterization is determined by the energy-containing scale itself. On the other hand, if the energy-containing scale is resolved—which may be the case in eddy-permitting models now being used for climate studies (Adcroft et al. 2019)—the vertical structure parameterization is determined by the largest unresolved scale that is proportional to the horizontal grid spacing. This parameterization is shown to capture the vertical structure of EKE filtered with different horizontal scales, so that it can be useful for both noneddying and eddy-permitting simulations.

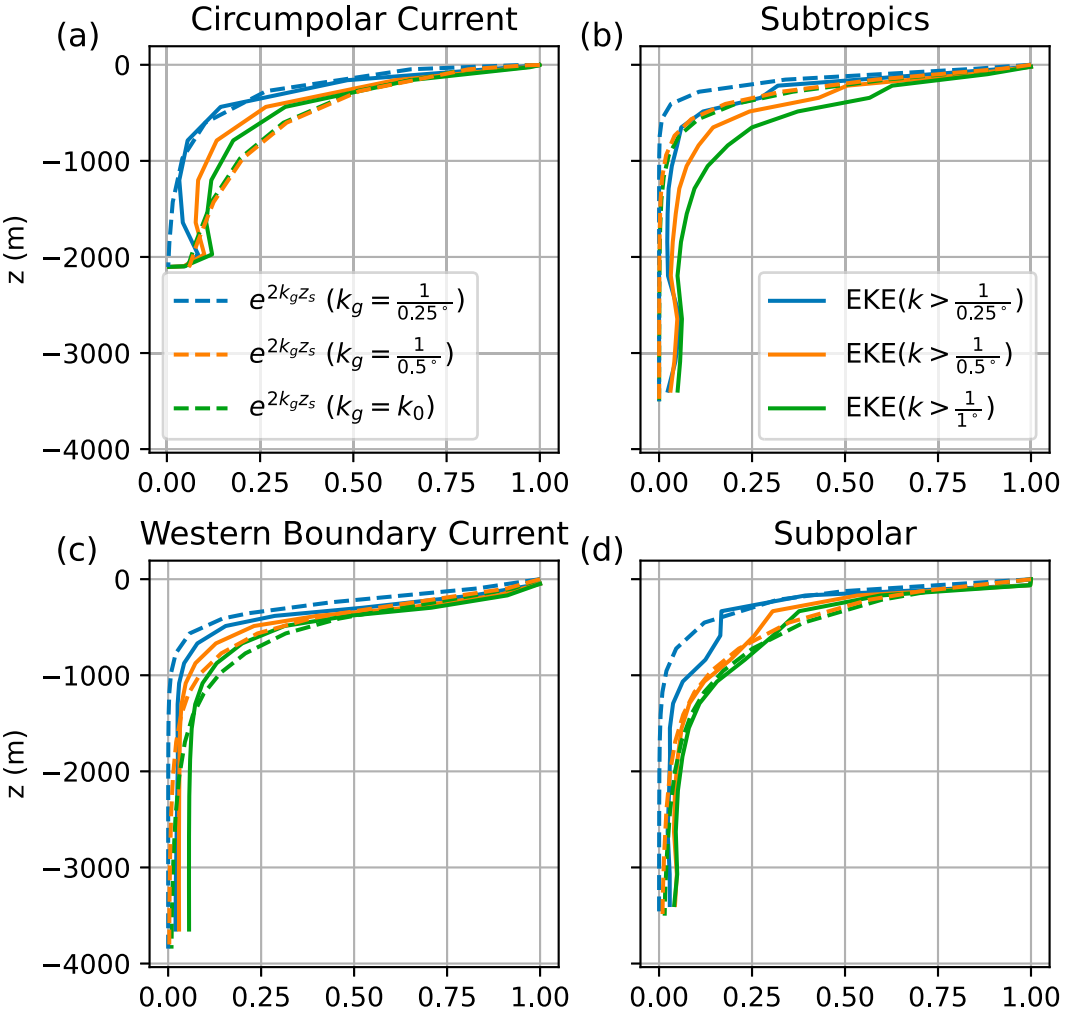

FIG. 12. The vertical structure of spatially filtered EKE in the four regions shown in Fig. 4. Blue, orange, and green solid lines are the high-pass filtered vertical structures of EKE with cutoff wavenumber as 1/0.25°, 1/0.5°, and 1/1°, respectively. They represent the vertical structures of subgrid EKE that is unresolved by 0.25°, 0.5°, and 1° models, assuming that a minimum of six grid points is required to resolve an eddy. All EKE profiles are normalized by their surface values. Blue, orange, and green dashed lines are the parameterized vertical structure $E_p(z, \Delta)$. The E_p depends on the model grid spacing Δ and the energy-containing wavenumber k_0. The vertical structure of subgrid EKE is determined by Δ at 0.25° and 0.5° resolutions, where the energy-containing eddy is resolved, and by k_0 at 1° resolution. The parameterization captures the scale dependence reasonably well, except for an underestimation in the subtropical region.

Full closure of the vertical structure parameterization requires a prediction of the horizontal energy-containing scale. The energy-containing scale is associated with the mechanism that halts the inverse energy cascade, for example, bottom friction and the planetary vorticity gradient (Rhines 1975; Larichev and Held 1995). Prediction of such an eddy length scale has been the focus of many studies (Larichev and Held 1995; Held and Larichev 1996; Thompson and Young 2006; Jansen et al. 2015; Kong and Jansen 2017; Chang and Held 2019; Gallet and Ferrari 2020; Chang and Held 2021; Gallet and Ferrari 2021).

The SQG mode does not fully capture the vertical structure of EKE in the lower latitudes and tropics. Previous studies reveal that the scaling for eddy mixing is different between the tropics and midlatitude ocean due to the dominance of linear waves (tropics) versus nonlinear eddies (extratropics) (Klocker and Abernathey 2014; Zhang and Wolfe 2022). Parameterization of the eddy vertical structure in the tropics requires additional work, though eddies there are mostly large enough to be well resolved by models targeted for climate simulations in the near future such as Adcroft et al. (2019).

c. *Prospects and future work*

Many previous studies consider the importance of bottom topography in causing the surface intensification of ocean eddies (Aoki et al. 2009; de La Lama et al. 2016; LaCasce 2017; Quan et al. 2023). Bottom topography can decouple abyssal

eddies from upper-ocean eddies, leading to baroclinic modes with zero horizontal velocity at the bottom (Rhines 1970; Samelson 1992; Hallberg 1997; Bobrovich and Reznik 1999; Tailleux and McWilliams 2001). We find that the first rough-bottom mode (the EBT mode), with zero horizontal velocity at the bottom, does not describe the vertical structure of EKE well in our simulation. This limitation arises from the EBT mode's ignorance of the surface buoyancy anomaly, which we find to be essential for reconstructing the eddy vertical structure. In fact, both the surface buoyancy and bottom topography can be incorporated in the general boundary conditions, described by Eq. (6), of vertical modes (LaCasce 2017; Yassin and Griffies 2022a). The vertical mode accounting for both effects will be explored in future work.

The model used in this study does not have a mixed layer, which can change the quantitative analyses of the instability and eddy energetics but, we expect, will not qualitatively change the role of surface PV in the vertical structure. Mixed layer baroclinic instability provides another important energy source for submesoscale eddies, which can cascade their energy upscale to energize mesoscale eddies (e.g., Fox-Kemper et al. 2008; Sasaki et al. 2014; Callies et al. 2016; Schubert et al. 2020; Dong et al. 2020; Khatri et al. 2021). Callies et al. (2016) show that the energy generated by mixed layer instability resides in the SQG mode, where the energy cascades upscale to the largest, most energetic eddies. This energy cascade is similar to our finding, with the difference that the SQG mode is mainly excited by the surface Charney instability in our model. The mixed-layer instability thus may play a similar role to the Charney instability in enhancing the surface-trapped mode. In a more realistic numerical setup, the mixed layer and Charney instabilities can coexist, with the relative importance between them depending on the depth of the mixed layer, stratification, and lateral buoyancy gradient in the upper ocean (Capet et al. 2016; Zhang et al. 2023).

This study serves as a step forward to understand and parameterize the eddy vertical structure by emphasizing its dependence on the horizontal scale, resulting from the impact of surface PV. The parameterization, described by Eq. (22), is ripe to be tested in noneddying and eddy-permitting simulations after combining it with a closure of the horizontal energy-containing scale (e.g., Jansen et al. 2015, 2019). We are planning to apply this vertical structure to the kinetic energy backscatter parameterization that has recently been used in both idealized and realistic eddy-permitting simulations (Jansen et al. 2019; Juricke et al. 2019, 2020; Yankovsky et al. 2024, manuscript submitted to *J. Adv. Model. Earth Syst.*; Chang et al. 2023). Other aspects, including the impacts of bottom topography and mixed layer, will also be incorporated in this scheme to predict the eddy vertical structure in more realistic situations.

As the Surface Water Ocean Topography (SWOT) satellite has become operational, the SQG schemes proposed here [Eqs. (15) or (17)] can be a useful tool for reconstructing the upper-ocean eddy fields using the sea surface height field from SWOT. Since the surface-intensified Charney instability has been found to be prevalent in the midlatitude oceans, particularly during the spring and winter (Capet et al. 2016; Feng et al. 2021, 2022), our schemes are physically justified to interpret and infer the eddy vertical structure in these regions. Such schemes can be evaluated by comparing to observations of the full-depth eddy profile (Ni et al. 2023).

Acknowledgments. We thank Alistair Adcroft, Laure Zanna, Chiung-Yin Chang, Jacob Steinberg, and Matthew Lobo for comments on drafts of this manuscript, as well as Elizabeth Yankovsky, Malte Jansen, Shafer Smith, and Baylor Fox-Kemper for helpful discussion. We also thank the two anonymous reviewers for their insightful comments that greatly improved the presentation. This work was supported by Award NA18OAR4320123 from the National Oceanic and Atmospheric Administration, U.S. Department of Commerce. The statements, findings, conclusions, and recommendations are those of the author(s) and do not necessarily reflect the views of the National Oceanic and Atmospheric Administration, or the U.S. Department of Commerce. W. Z. and C. L. P. W. were also supported by the NSF (OCE-2048826). Computing and data storage resources, including the Cheyenne supercomputer (https://doi.org/10.5065/D6RX99HX), were provided by the Computational and Information Systems Laboratory at NCAR, under NCAR/CISL Project Number UNYU0004.

Data availability statement. The model, NeverWorld2, dataset and detailed information on its configuration are available at https://doi.org/10.26024/f130-ev71 (Marques et al. 2022).

APPENDIX A

Comparison of the Surface-Trapped Mode to the Solution in Lapeyre and Klein (2006)

The orthogonal basis derived from Eqs. (8) and (9) is different from that in Lapeyre and Klein (2006). They proposed a decomposition of the eddy streamfunction ψ into a surface component ψ_{sur} satisfying

$$\begin{aligned} \nabla^2\psi_{\mathrm{sur}} + \frac{\partial}{\partial z}\left(\frac{f^2}{N^2}\frac{\partial\psi_{\mathrm{sur}}}{\partial z}\right) &= 0, \\ \left.\frac{\partial\psi_{\mathrm{sur}}}{\partial z}\right|_{z=0} &= \frac{b_s}{f}, \\ \left.\frac{\partial\psi_{\mathrm{sur}}}{\partial z}\right|_{z=-H} &= 0, \end{aligned} \tag{A1}$$

and an interior component ψ_{int} satisfying

$$\begin{aligned} \nabla^2\psi_{\mathrm{int}} + \frac{\partial}{\partial z}\left(\frac{f^2}{N^2}\frac{\partial\psi_{\mathrm{int}}}{\partial z}\right) &= q, \\ \left.\frac{\partial\psi_{\mathrm{int}}}{\partial z}\right|_{z=0} &= 0, \\ \left.\frac{\partial\psi_{\mathrm{int}}}{\partial z}\right|_{z=-H} &= 0. \end{aligned} \tag{A2}$$

Here, b_s is the surface buoyancy anomaly and q is the PV, with the bottom boundary condition specified following Lapeyre (2009). Note that in Eqs. (8) and (9), we use Φ for the vertical mode in contrast to ψ_{sur} and ψ_{int} here.

The interior solution ψ_{int} is driven by interior PV anomalies and can be projected onto the flat-bottom modes satisfying Eqs. (3) and (4). The surface solution ψ_{sur} is driven by surface buoyancy anomalies. Although ψ_{sur} and the surface-trapped mode Φ_s [described by Eq. (8)] share certain properties (i.e., zero interior PV anomaly and horizontal wavenumber dependence), they satisfy different surface boundary conditions—ψ_{sur} satisfies a Neumann surface boundary condition (i.e., surface buoyancy anomaly is given), while Φ_s satisfies a Dirichlet surface boundary condition (i.e., surface pressure anomaly is given). The derivation of Φ_s [Eq. (8)] indicates that when the mean surface PV gradient becomes much stronger than the interior gradient, the surface-trapped mode Φ_s will dominate the surface pressure anomaly, while interior modes Φ_m will have zero surface pressure anomaly. We call Φ_s as the SQG mode because it has zero interior PV anomaly and is dynamically driven by the surface buoyancy/PV anomaly, while interior modes Φ_m are driven by both surface and interior PV anomalies.

Although ψ_{sur} of Lapeyre and Klein (2006) uses surface buoyancy anomaly as the boundary condition, later studies have modified its surface boundary condition to incorporate surface pressure (or SSH) anomaly and finding such a formulation (i.e., Φ_s) successfully reconstructs the vertical profile of EKE and vertical velocity in both idealized and realistic ocean simulations (Klein et al. 2009; Isern-Fontanet et al. 2008; Qiu et al. 2016, 2020). Conversely, studies employing ψ_{sur}, estimated from surface buoyancy anomaly, reveal its limited contribution in reconstructing the eddy vertical structure (Wang et al. 2013; LaCasce and Wang 2015). Isern-Fontanet et al. (2008) find that ψ_{sur} reconstructs the vertical structure of buoyancy and velocity well only in the upper 100–200 m, while Φ_s reconstructs the buoyancy and velocity well from the base of the mixed layer to at least 1000 m in the North Atlantic Ocean (their Figs. 8 and 9). They attribute the error of ψ_{sur} to the deviation of surface buoyancy from its value at the base of the mixed layer due to the presence of mixed layer processes.

APPENDIX B

Surface PV in Layered Quasigeostrophic Models

Eddies in the shallow-water model, described in section 3a, are analyzed based on layered QG dynamics. The eddy streamfunction ψ can be obtained from the distribution of the QG PV, q, by inverting the relation:

$$
\begin{aligned}
q_1 &= \nabla^2\psi_1 + \frac{f^2}{H_1}\frac{\psi_2 - \psi_1}{g_1'},\\
q_n &= \nabla^2\psi_n + \frac{f^2}{H_n}\left(\frac{\psi_{n-1} - \psi_n}{g_{n-1}'} - \frac{\psi_n - \psi_{n+1}}{g_n'}\right),\ n \in [2, n_m - 1],\\
q_{n_m} &= \nabla^2\psi_{n_m} + \frac{f^2}{H_{n_m}}\frac{\psi_{n_m-1} - \psi_{n_m}}{g_{n_m-1}'},
\end{aligned}
\tag{B1}
$$

where $(\cdot)_n$ indicates the property on the nth layer, H_n is the layer thickness, f is the Coriolis parameter, $n_m = 15$ for our simulations, and g_n' is the reduced gravity, computed as

$$
g_n' = g\frac{\rho_{n+1} - \rho_n}{\rho_0}, \tag{B2}
$$

where $g = 10\ \text{m}^2\ \text{s}^{-1}$, ρ_n is the uniform layer density, and $\rho_0 = 1000\ \text{kg}\ \text{m}^{-3}$ is the reference density. We emphasize that n in this paper is used to label the discrete layer number in the stacked shallow-water model, whereas m was introduced earlier and denotes the vertical eigenmode.

In matrix form, the relationship between $\mathcal{Q} = [q_1,\ldots,q_{n_m}]^{\text{T}}$ and $\boldsymbol{\psi} = [\psi_1,\ldots,\psi_{n_m}]^{\text{T}}$ can be written as

$$
\mathcal{Q} = (\mathbb{S} + \mathbb{I}\nabla^2)\boldsymbol{\psi}, \tag{B3}
$$

where $\mathbb{I}$ is the $N \times N$ identity matrix and $\mathbb{S}$ is the stretching matrix written as

$$
\mathbb{S} = f^2\begin{bmatrix}
-\dfrac{1}{H_1 g_1'} & \dfrac{1}{H_1 g_1'} & 0 & 0 & \cdots\\
\vdots & \vdots & & \vdots & \\
\cdots & \dfrac{1}{H_n g_{n-1}'} & -\dfrac{1}{H_n g_{n-1}'} - \dfrac{1}{H_n g_n'} & \dfrac{1}{H_n g_n'} & \cdots\\
\vdots & \vdots & & \vdots & \\
\cdots & 0 & 0 & \dfrac{1}{H_{n_m} g_{n_m-1}'} & -\dfrac{1}{H_{n_m} g_{n_m-1}'}
\end{bmatrix}
$$

Surface buoyancy is not explicitly simulated in a stacked shallow-water model. Even so, its dynamical impact is similar to that of the surface-layer PV, q_1. The streamfunction due to SQG dynamics $\boldsymbol{\psi}_s$ is equivalent to the streamfunction induced by the surface-layer PV,

$$
\boldsymbol{\psi}_s = (\mathbb{S} + \mathbb{I}\nabla^2)^{-1}\mathcal{Q}_s, \tag{B4}
$$

where $\mathcal{Q}_s = [q_1,0,\ldots,0]^{\text{T}}$.

APPENDIX C

Linear Stability Analysis

The QG PV evolution equation in a layered QG model (e.g., Vallis 2017) is

$$\left(\frac{\partial}{\partial t} + \mathbf{U}_n \cdot \nabla\right) q_n + J(\psi_n, q_n) + J(\psi_n, Q_n) = 0, \tag{C1}$$

where J is the Jacobian, $\mathbf{U} = U\mathbf{i} + V\mathbf{j}$, U and V are the background zonal and meridional velocities, and Q is the background PV estimated as

$$\mathbb{Q} = \mathbb{S}\mathbb{V}x + (\beta - \mathbb{S}\mathbb{U})y, \tag{C2}$$

where $\mathbb{Q} = [Q_1,...,Q_{n_m}]^{\mathrm{T}}$, $\mathbb{U} = [U_1,...,U_{n_m}]^{\mathrm{T}}$, and $\mathbb{V} = [V_1, ..., V_{n_m}]^{\mathrm{T}}$. Zonal and meridional background PV gradients, Q_x and Q_y, respectively, are

$$\begin{aligned} \mathbb{Q}_x &= \mathbb{S}\mathbb{V}, \\ \mathbb{Q}_y &= \beta - \mathbb{S}\mathbb{U}. \end{aligned} \tag{C3}$$

Inserting a wave ansatz, $\psi_n = \mathrm{Re}[\hat{\psi}_n e^{i(k_x x + k_y y - \omega t)}]$, into the linearized PV Eq. (C1), we get

$$i(k_x U_n + k_y V_n - \omega)\hat{q}_n + (ik_x Q_{ny} - ik_y Q_{nx})\hat{\psi}_n = 0, \tag{C4}$$

where the relationship between $\hat{\mathcal{Q}} = [\hat{q}_1,...,\hat{q}_{n_m}]^{\mathrm{T}}$ and $\hat{\boldsymbol{\psi}} = [\hat{\psi}_1,...,\hat{\psi}_{n_m}]^{\mathrm{T}}$ is given by Eq. (B3),

$$\hat{\mathcal{Q}} = (\mathbb{S} - k^2\mathbb{I})\hat{\boldsymbol{\psi}}, \tag{C5}$$

Equation (C4) forms a generalized eigenvalue problem for the mode $\hat{\boldsymbol{\psi}}$ (eigenvectors) and the angular frequency ω (eigenvalues),

$$\omega\mathbb{A}\hat{\boldsymbol{\psi}} = \mathbb{C}\hat{\boldsymbol{\psi}}, \tag{C6}$$

where $\mathbb{A} = \mathbb{S} - k^2\mathbb{I}$, $C_{ij} = (k_x U_n + k_y V_n)\delta_{inm}A_{mj} + (k_x Q_{ny} - k_y Q_{nx})\delta_{ijn}$, and δ is the Kronecker delta function.

APPENDIX D

Analogy to Continuous QG Model

The surface PV and linear stability analysis described in appendixes B and C are for a layered QG framework, which is a natural fit for the shallow-water model used in this study. One may wonder how these equations are relevant to those in a model with continuous stratification. Here, we derive the vertically discretized form of the continuous QG equations and show that they are equivalent to the layered QG equations and the surface buoyancy anomaly can be absorbed into the surface-layer PV.

The linear stability problem in continuous QG is

$$\left(\frac{\partial}{\partial t} + \mathbf{U} \cdot \nabla\right) q + \mathbf{u} \cdot \nabla Q = 0, \quad -H < z < 0 \tag{D1}$$

where the eddy PV is $q = \nabla^2\psi + \partial_z[(f^2/N^2)\partial_z\psi]$, the mean PV is $Q = \beta y + \partial_z[(f/N^2)B]$, and geostrophic velocity is $\mathbf{u} = \mathbf{k} \times \nabla\psi$. The boundary conditions are applied to the buoyancy anomaly $b = f\partial_z\psi$,

$$\left(\frac{\partial}{\partial t} + \mathbf{U} \cdot \nabla\right) b + \mathbf{u} \cdot \nabla B = 0, \quad z = -H, \ 0. \tag{D2}$$

Discretizing Eq. (D1) in the vertical direction for n_m vertical layers, we get for $n \in [1, n_m]$

$$\left(\frac{\partial}{\partial t} + \mathbf{U}_n \cdot \nabla\right)\left[\nabla^2\psi_n + \frac{f^2}{\Delta z_n}\left(\frac{\psi_{n-1} - \psi_n}{N^2_{n-(1/2)}\Delta z_{n-(1/2)}} - \frac{\psi_n - \psi_{n+1}}{N^2_{n+(1/2)}\Delta z_{n+(1/2)}}\right)\right] + \beta v_n + \mathbf{u}_n \cdot \nabla\left(\frac{f}{\Delta z_n N^2_{n-(1/2)}}B_{n-(1/2)} - \frac{f}{\Delta z_n N^2_{n+(1/2)}}B_{n+(1/2)}\right) = 0, \tag{D3}$$

with the boundary conditions (D2) discretized as

$$\left(\frac{\partial}{\partial t} + \mathbf{U}_1 \cdot \nabla\right)\frac{f(\psi_0 - \psi_1)}{\Delta z_{1/2}} + \mathbf{u}_1 \cdot \nabla B_{1/2} = 0, \tag{D4}$$

$$\left(\frac{\partial}{\partial t} + \mathbf{U}_{n_m} \cdot \nabla\right)\frac{f(\psi_{n_m} - \psi_{n_m+1})}{\Delta z_{n_m+(1/2)}} + \mathbf{u}_{n_m} \cdot \nabla B_{n_m+(1/2)} = 0, \tag{D5}$$

where $n = 1/2$ and $n = n_m + 1/2$ indicate the upper and lower boundaries, respectively, and ψ_0 and ψ_{n_m+1} are the eddy streamfunctions at the upper and lower boundaries, respectively. Here, we have assumed that the buoyancy at the upper (lower) boundary is advected by the same flows in the top (bottom) layers.

By inserting $f/(N^2_{1/2}\Delta z_1) \times$ (D4) and $f/[N^2_{n_m+(1/2)}\Delta z_{n_m}] \times$ (D5) into Eq. (D3), we get

$$\left(\frac{\partial}{\partial t} + \mathbf{U}_n \cdot \nabla\right) q_n + \mathbf{u}_n \cdot \nabla Q_n = 0, \tag{D6}$$

where the eddy PV q_n is

$$\begin{aligned} q_1 &= \nabla^2\psi_1 + \frac{f^2}{\Delta z_1}\frac{\psi_2 - \psi_1}{N^2_{3/2}\Delta z_{3/2}}, \\ q_n &= \nabla^2\psi_n + \frac{f^2}{\Delta z_n}\left[\frac{\psi_{n-1} - \psi_n}{N^2_{n-(1/2)}\Delta z_{n-(1/2)}} - \frac{\psi_n - \psi_{n+1}}{N^2_{n+(1/2)}\Delta z_{n+(1/2)}}\right], \ n \in [2, n_m - 1], \\ q_{n_m} &= \nabla^2\psi_{n_m} + \frac{f^2}{\Delta z_{n_m}}\frac{\psi_{n_m-1} - \psi_{n_m}}{N^2_{n_m-(1/2)}\Delta z_{n_m-(1/2)}}, \end{aligned} \tag{D7}$$

and the mean PV Q_n is

$$
\begin{aligned}
Q_1 &= \beta y - \frac{fB_{3/2}}{N_{3/2}^2 \Delta z_1},\\
Q_n &= \beta y + \frac{f}{\Delta z_n}\left[\frac{B_{n-(1/2)}}{N_{n-(1/2)}^2} - \frac{B_{n+(1/2)}}{N_{n+(1/2)}^2}\right],\\
Q_{n_m} &= \beta y + \frac{fB_{n_m-(1/2)}}{N_{n_m-(1/2)}^2 \Delta z_{n_m}}.
\end{aligned}
\tag{D8}
$$

The boundary conditions are absorbed into the discretized PV equation [Eq. (D6)], where the buoyancy anomaly (mean buoyancy gradient) at the upper and lower boundaries are absorbed into the PV anomaly (mean PV gradient) in the top and bottom layers, respectively. Recall that $g' = N^2 \Delta z$ and $\nabla B = \mathbf{k} \times f\partial_z \mathbf{U}$, Eqs. (D7) and (D8) are equivalent to the eddy and mean PV in layered QG, expressed by Eqs. (B3) and (C3), respectively.

REFERENCES

Adcroft, A., and Coauthors, 2019: The GFDL global ocean and sea ice model OM4.0: Model description and simulation features. *J. Adv. Model. Earth Syst.*, **11**, 3167–3211, https://doi.org/10.1029/2019MS001726.

Ajayi, A., J. Le Sommer, E. Chassignet, J.-M. Molines, X. Xu, A. Albert, and E. Cosme, 2020: Spatial and temporal variability of the North Atlantic eddy field from two kilometric-resolution ocean models. *J. Geophys. Res. Oceans*, **125**, e2019JC015827, https://doi.org/10.1029/2019JC015827.

Aoki, K., A. Kubokawa, H. Sasaki, and Y. Sasai, 2009: Midlatitude baroclinic Rossby waves in a high-resolution OGCM simulation. *J. Phys. Oceanogr.*, **39**, 2264–2279, https://doi.org/10.1175/2009JPO4137.1.

Blumen, W., 1978: Uniform potential vorticity flow: Part I. Theory of wave interactions and two-dimensional turbulence. *J. Atmos. Sci.*, **35**, 774–783, https://doi.org/10.1175/1520-0469(1978)035<0774:UPVFPI>2.0.CO;2.

Bobrovich, A. V., and G. M. Reznik, 1999: Planetary waves in a stratified ocean of variable depth. Part 2. Continuously stratified ocean. *J. Fluid Mech.*, **388**, 147–169, https://doi.org/10.1017/S0022112099004863.

Bretherton, F. P., 1966: Critical layer instability in baroclinic flows. *Quart. J. Roy. Meteor. Soc.*, **92**, 325–334, https://doi.org/10.1002/qj.49709239302.

Brink, K. H., and J. Pedlosky, 2020: The structure of baroclinic modes in the presence of baroclinic mean flow. *J. Phys. Oceanogr.*, **50**, 239–253, https://doi.org/10.1175/JPO-D-19-0123.1.

Callies, J., G. Flierl, R. Ferrari, and B. Fox-Kemper, 2016: The role of mixed-layer instabilities in submesoscale turbulence. *J. Fluid Mech.*, **788**, 5–41, https://doi.org/10.1017/jfm.2015.700.

Capet, X., J. C. McWilliams, M. J. Molemaker, and A. F. Shchepetkin, 2008: Mesoscale to submesoscale transition in the California Current System. Part III: Energy balance and flux. *J. Phys. Oceanogr.*, **38**, 2256–2269, https://doi.org/10.1175/2008JPO3810.1.

——, G. Roullet, P. Klein, and G. Maze, 2016: Intensification of upper-ocean submesoscale turbulence through Charney baroclinic instability. *J. Phys. Oceanogr.*, **46**, 3365–3384, https://doi.org/10.1175/JPO-D-16-0050.1.

Chang, C.-Y., and I. M. Held, 2019: The control of surface friction on the scales of baroclinic eddies in a homogeneous quasigeostrophic two-layer model. *J. Atmos. Sci.*, **76**, 1627–1643, https://doi.org/10.1175/JAS-D-18-0333.1.

——, and ——, 2021: The parameter dependence of eddy heat flux in a homogeneous quasigeostrophic two-layer model on a β plane with quadratic friction. *J. Atmos. Sci.*, **78**, 97–106, https://doi.org/10.1175/JAS-D-20-0145.1.

——, A. Adcroft, L. Zanna, R. W. Hallberg, and S. M. Griffies, 2023: Remote versus local impacts of energy backscatter on the North Atlantic SST biases in a global ocean model. *Geophys. Res. Lett.*, **50**, e2023GL105757, https://doi.org/10.1029/2023GL105757.

Charney, J. G., 1947: The dynamics of long waves in a baroclinic westerly current. *J. Atmos. Sci.*, **4**, 136–162, https://doi.org/10.1175/1520-0469(1947)004<0136:TDOLWI>2.0.CO;2.

——, 1971: Geostrophic turbulence. *J. Atmos. Sci.*, **28**, 1087–1095, https://doi.org/10.1175/1520-0469(1971)028<1087:GT>2.0.CO;2.

Chelton, D. B., M. G. Schlax, and R. M. Samelson, 2011: Global observations of nonlinear mesoscale eddies. *Prog. Oceanogr.*, **91**, 167–216, https://doi.org/10.1016/j.pocean.2011.01.002.

Danabasoglu, G., and J. Marshall, 2007: Effects of vertical variations of thickness diffusivity in an ocean general circulation model. *Ocean Modell.*, **18**, 122–141, https://doi.org/10.1016/j.ocemod.2007.03.006.

de La Lama, M. S., J. H. LaCasce, and H. K. Fuhr, 2016: The vertical structure of ocean eddies. *Dyn. Stat. Climate Syst.*, **1**, dzw001, https://doi.org/10.1093/climsys/dzw001.

Dong, J., B. Fox-Kemper, H. Zhang, and C. Dong, 2020: The seasonality of submesoscale energy production, content, and cascade. *Geophys. Res. Lett.*, **47**, e2020GL087388, https://doi.org/10.1029/2020GL087388.

Eady, E. T., 1949: Long waves and cyclone waves. *Tellus*, **1**, 33–52, https://doi.org/10.3402/tellusa.v1i3.8507.

Eden, C., M. Jochum, and G. Danabasoglu, 2009: Effects of different closures for thickness diffusivity. *Ocean Modell.*, **26**, 47–59, https://doi.org/10.1016/j.ocemod.2008.08.004.

Feng, L., C. Liu, A. Köhl, D. Stammer, and F. Wang, 2021: Four types of baroclinic instability waves in the global oceans and the implications for the vertical structure of mesoscale eddies. *J. Geophys. Res. Oceans*, **126**, e2020JC016966, https://doi.org/10.1029/2020JC016966.

——, ——, ——, and F. Wang, 2022: Seasonality of four types of baroclinic instability in the global oceans. *J. Geophys. Res. Oceans*, **127**, e2022JC018572, https://doi.org/10.1029/2022JC018572.

Ferrari, R., and C. Wunsch, 2009: Ocean circulation kinetic energy: Reservoirs, sources, and sinks. *Annu. Rev. Fluid Mech.*, **41**, 253–282, https://doi.org/10.1146/annurev.fluid.40.111406.102139.

Fox-Kemper, B., R. Ferrari, and R. Hallberg, 2008: Parameterization of mixed layer eddies. Part I: Theory and diagnosis. *J. Phys. Oceanogr.*, **38**, 1145–1165, https://doi.org/10.1175/2007JPO3792.1.

Frenger, I., M. Münnich, N. Gruber, and R. Knutti, 2015: Southern Ocean eddy phenomenology. *J. Geophys. Res. Oceans*, **120**, 7413–7449, https://doi.org/10.1002/2015JC011047.

Fresnay, S., A. L. Ponte, S. Le Gentil, and J. Le Sommer, 2018: Reconstruction of the 3-D dynamics from surface variables in a high-resolution simulation of North Atlantic. *J. Geophys. Res. Oceans*, **123**, 1612–1630, https://doi.org/10.1002/2017JC013400.

Fu, L.-L., and G. R. Flierl, 1980: Nonlinear energy and enstrophy transfers in a realistically stratified ocean. *Dyn. Atmos. Oceans*, **4**, 219–246, https://doi.org/10.1016/0377-0265(80)90029-9.

Gallet, B., and R. Ferrari, 2020: The vortex gas scaling regime of baroclinic turbulence. *Proc. Natl. Acad. Sci. USA*, **117**, 4491–4497, https://doi.org/10.1073/pnas.1916272117.

——, and ——, 2021: A quantitative scaling theory for meridional heat transport in planetary atmospheres and oceans. *AGU Adv.*, **2**, e2020AV000362, https://doi.org/10.1029/2020AV000362.

Gill, A., 1982: *Atmosphere–Ocean Dynamics*. International Geophysics Series, Vol. 30, Academic Press, 662 pp.

Gnanadesikan, A., M.-A. Pradal, and R. Abernathey, 2015: Isopycnal mixing by mesoscale eddies significantly impacts oceanic anthropogenic carbon uptake. *Geophys. Res. Lett.*, **42**, 4249–4255, https://doi.org/10.1002/2015GL064100.

Griffies, S. M., and R. W. Hallberg, 2000: Biharmonic friction with a Smagorinsky-like viscosity for use in large-scale eddy-permitting ocean models. *Mon. Wea. Rev.*, **128**, 2935–2946, https://doi.org/10.1175/1520-0493(2000)128<2935:BFWASL>2.0.CO;2.

——, and Coauthors, 2015: Impacts on ocean heat from transient mesoscale eddies in a hierarchy of climate models. *J. Climate*, **28**, 952–977, https://doi.org/10.1175/JCLI-D-14-00353.1.

Groeskamp, S., J. H. LaCasce, T. J. McDougall, and M. Rogé, 2020: Full-depth global estimates of ocean mesoscale eddy mixing from observations and theory. *Geophys. Res. Lett.*, **47**, e2020GL089425, https://doi.org/10.1029/2020GL089425.

Hallberg, R., 1997: Localized coupling between surface and bottom-intensified flow over topography. *J. Phys. Oceanogr.*, **27**, 977–998, https://doi.org/10.1175/1520-0485(1997)027<0977:LCBSAB>2.0.CO;2.

Hausmann, U., and A. Czaja, 2012: The observed signature of mesoscale eddies in sea surface temperature and the associated heat transport. *Deep-Sea Res. I*, **70**, 60–72, https://doi.org/10.1016/j.dsr.2012.08.005.

Held, I. M., and V. D. Larichev, 1996: A scaling theory for horizontally homogeneous, baroclinically unstable flow on a beta plane. *J. Atmos. Sci.*, **53**, 946–952, https://doi.org/10.1175/1520-0469(1996)053<0946:ASTFHH>2.0.CO;2.

——, R. T. Pierrehumbert, S. T. Garner, and K. L. Swanson, 1995: Surface quasi-geostrophic dynamics. *J. Fluid Mech.*, **282**, 1–20, https://doi.org/10.1017/S0022112095000012.

Holmes, R. M., S. Groeskamp, K. D. Stewart, and T. J. McDougall, 2022: Sensitivity of a coarse-resolution global ocean model to a spatially variable neutral diffusivity. *J. Adv. Model. Earth Syst.*, **14**, e2021MS002914, https://doi.org/10.1029/2021MS002914.

Isern-Fontanet, J., G. Lapeyre, P. Klein, B. Chapron, and M. W. Hecht, 2008: Three-dimensional reconstruction of oceanic mesoscale currents from surface information. *J. Geophys. Res.*, **113**, C09005, https://doi.org/10.1029/2007JC004692.

Jansen, M. F., A. J. Adcroft, R. Hallberg, and I. M. Held, 2015: Parameterization of eddy fluxes based on a mesoscale energy budget. *Ocean Modell.*, **92**, 28–41, https://doi.org/10.1016/j.ocemod.2015.05.007.

——, A. Adcroft, S. Khani, and H. Kong, 2019: Toward an energetically consistent, resolution aware parameterization of ocean mesoscale eddies. *J. Adv. Model. Earth Syst.*, **11**, 2844–2860, https://doi.org/10.1029/2019MS001750.

Juricke, S., S. Danilov, A. Kutsenko, and M. Oliver, 2019: Ocean kinetic energy backscatter parametrizations on unstructured grids: Impact on mesoscale turbulence in a channel. *Ocean Modell.*, **138**, 51–67, https://doi.org/10.1016/j.ocemod.2019.03.009.

——, ——, N. Koldunov, M. Oliver, and D. Sidorenko, 2020: Ocean kinetic energy backscatter parametrization on unstructured grids: Impact on global eddy-permitting simulations. *J. Adv. Model. Earth Syst.*, **12**, e2019MS001855, https://doi.org/10.1029/2019MS001855.

Keffer, T., 1985: The ventilation of the World's oceans: Maps of the potential vorticity field. *J. Phys. Oceanogr.*, **15**, 509–523, https://doi.org/10.1175/1520-0485(1985)015<0509:TVOTWO>2.0.CO;2.

Khatri, H., S. M. Griffies, T. Uchida, H. Wang, and D. Menemenlis, 2021: Role of mixed-layer instabilities in the seasonal evolution of eddy kinetic energy spectra in a global submesoscale permitting simulation. *Geophys. Res. Lett.*, **48**, e2021GL094777, https://doi.org/10.1029/2021GL094777.

Killworth, P. D., 1992: An equivalent-barotropic mode in the fine resolution Antarctic model. *J. Phys. Oceanogr.*, **22**, 1379–1387, https://doi.org/10.1175/1520-0485(1992)022<1379:AEBMIT>2.0.CO;2.

Klein, P., J. Isern-Fontanet, G. Lapeyre, G. Roullet, E. Danioux, B. Chapron, S. Le Gentil, and H. Sasaki, 2009: Diagnosis of vertical velocities in the upper ocean from high resolution sea surface height. *Geophys. Res. Lett.*, **36**, L12603, https://doi.org/10.1029/2009GL038359.

Klocker, A., and R. Abernathey, 2014: Global patterns of mesoscale eddy properties and diffusivities. *J. Phys. Oceanogr.*, **44**, 1030–1046, https://doi.org/10.1175/JPO-D-13-0159.1.

Kong, H., and M. F. Jansen, 2017: The eddy diffusivity in barotropic β-plane turbulence. *Fluids*, **2**, 54, https://doi.org/10.3390/fluids2040054.

LaCasce, J. H., 2017: The prevalence of oceanic surface modes. *Geophys. Res. Lett.*, **44**, 11 097–11 105, https://doi.org/10.1002/2017GL075430.

——, and A. Mahadevan, 2006: Estimating subsurface horizontal and vertical velocities from sea-surface temperature. *J. Mar. Res.*, **64**, 695–721, https://doi.org/10.1357/002224006779367267.

——, and J. Wang, 2015: Estimating subsurface velocities from surface fields with idealized stratification. *J. Phys. Oceanogr.*, **45**, 2424–2435, https://doi.org/10.1175/JPO-D-14-0206.1.

Lapeyre, G., 2009: What vertical mode does the altimeter reflect? On the decomposition in baroclinic modes and on a surface-trapped mode. *J. Phys. Oceanogr.*, **39**, 2857–2874, https://doi.org/10.1175/2009JPO3968.1.

——, 2017: Surface quasi-geostrophy. *Fluids*, **2**, 7, https://doi.org/10.3390/fluids2010007.

——, and P. Klein, 2006: Dynamics of the upper oceanic layers in terms of surface quasigeostrophy theory. *J. Phys. Oceanogr.*, **36**, 165–176, https://doi.org/10.1175/JPO2840.1.

Larichev, V. D., and I. M. Held, 1995: Eddy amplitudes and fluxes in a homogeneous model of fully developed baroclinic instability. *J. Phys. Oceanogr.*, **25**, 2285–2297, https://doi.org/10.1175/1520-0485(1995)025<2285:EAAFIA>2.0.CO;2.

Liu, L., S. Peng, J. Wang, and R. X. Huang, 2014: Retrieving density and velocity fields of the ocean's interior from surface data. *J. Geophys. Res. Oceans*, **119**, 8512–8529, https://doi.org/10.1002/2014JC010221.

——, ——, and R. X. Huang, 2017: Reconstruction of ocean's interior from observed sea surface information. *J. Geophys. Res. Oceans*, **122**, 1042–1056, https://doi.org/10.1002/2016JC011927.

Loose, N., G. M. Marques, A. Adcroft, S. D. Bachman, S. M. Griffies, I. Grooms, R. W. Hallberg, and M. F. Jansen, 2022: Parameterizing eddy form stress in a thickness-weighted average isopycnal ocean model. ESS Open Archive, 10512867.1, https://doi.org/10.1002/essoar.10512867.1.

Marques, G. M., and Coauthors, 2022: NeverWorld2: An idealized model hierarchy to investigate ocean mesoscale eddies across resolutions. *Geosci. Model Dev.*, **15**, 6567–6579, https://doi.org/10.5194/gmd-15-6567-2022.

Marshall, J., and K. Speer, 2012: Closure of the meridional overturning circulation through Southern Ocean upwelling. *Nat. Geosci.*, **5**, 171–180, https://doi.org/10.1038/ngeo1391.

Miracca-Lage, M., C. González-Haro, D. C. Napolitano, J. Isern-Fontanet, and P. S. Polito, 2022: Can the Surface Quasi-Geostrophic (SQG) theory explain upper ocean dynamics in the South Atlantic? *J. Geophys. Res. Oceans*, **127**, e2021JC018001, https://doi.org/10.1029/2021JC018001.

Ni, Q., X. Zhai, J. H. LaCasce, D. Chen, and D. P. Marshall, 2023: Full-depth eddy kinetic energy in the global ocean estimated from altimeter and Argo observations. *Geophys. Res. Lett.*, **50**, e2023GL103114, https://doi.org/10.1029/2023GL103114.

Pedlosky, J., 1996: Vertical structure: Baroclinic quasi-geostrophic models. *Ocean Circulation Theory*, Springer, 93–170.

Phillips, N. A., 1954: Energy transformations and meridional circulations associated with simple baroclinic waves in a two-level, quasi-geostrophic model. *Tellus*, **6A**, 274–286, https://doi.org/10.3402/tellusa.v6i3.8734.

Pierrehumbert, R. T., and K. L. Swanson, 1995: Baroclinic instability. *Annu. Rev. Fluid Mech.*, **27**, 419–467, https://doi.org/10.1146/annurev.fl.27.010195.002223.

Ponte, A. L., and P. Klein, 2013: Reconstruction of the upper ocean 3D dynamics from high-resolution sea surface height. *Ocean Dyn.*, **63**, 777–791, https://doi.org/10.1007/s10236-013-0611-7.

Qiu, B., S. Chen, P. Klein, C. Ubelmann, L.-L. Fu, and H. Sasaki, 2016: Reconstructability of three-dimensional upper-ocean circulation from SWOT sea surface height measurements. *J. Phys. Oceanogr.*, **46**, 947–963, https://doi.org/10.1175/JPO-D-15-0188.1.

——, ——, ——, H. Torres, J. Wang, L.-L. Fu, and D. Menemenlis, 2020: Reconstructing upper-ocean vertical velocity field from sea surface height in the presence of unbalanced motion. *J. Phys. Oceanogr.*, **50**, 55–79, https://doi.org/10.1175/JPO-D-19-0172.1.

Quan, Q., and Coauthors, 2023: Observed oceanic surface modes in the northern South China Sea. *J. Phys. Oceanogr.*, **53**, 1835–1849, https://doi.org/10.1175/JPO-D-22-0250.1.

Radko, T., 2023: A generalized theory of flow forcing by rough topography. *J. Fluid Mech.*, **961**, A24, https://doi.org/10.1017/jfm.2023.169.

Rhines, P., 1970: Edge-, bottom-, and Rossby waves in a rotating stratified fluid. *Geophys. Astrophys. Fluid Dyn.*, **1**, 273–302, https://doi.org/10.1080/03091927009365776.

Rhines, P. B., 1975: Waves and turbulence on a beta-plane. *J. Fluid Mech.*, **69**, 417–443, https://doi.org/10.1017/S0022112075001504.

——, and W. R. Young, 1982a: Homogenization of potential vorticity in planetary gyres. *J. Fluid Mech.*, **122**, 347–367, https://doi.org/10.1017/S0022112082002250.

——, and ——, 1982b: A theory of the wind-driven circulation. I. Mid-ocean gyres. *J. Mar. Res.*, **40**, 559–596.

Rocha, C. B., A. Tandon, I. C. A. da Silveira, and J. A. M. Lima, 2013: Traditional quasi-geostrophic modes and surface quasi-geostrophic solutions in the southwestern Atlantic. *J. Geophys. Res. Oceans*, **118**, 2734–2745, https://doi.org/10.1002/jgrc.20214.

——, W. R. Young, and I. Grooms, 2016: On Galerkin approximations of the surface active quasigeostrophic equations. *J. Phys. Oceanogr.*, **46**, 125–139, https://doi.org/10.1175/JPO-D-15-0073.1.

Roullet, G., J. C. Mcwilliams, X. Capet, and M. J. Molemaker, 2012: Properties of steady geostrophic turbulence with isopycnal outcropping. *J. Phys. Oceanogr.*, **42**, 18–38, https://doi.org/10.1175/JPO-D-11-09.1.

Salmon, R., 1980: Baroclinic instability and geostrophic turbulence. *Geophys. Astrophys. Fluid Dyn.*, **15**, 167–211, https://doi.org/10.1080/03091928008241178.

Samelson, R., 1992: Surface-intensified Rossby waves over rough topography. *J. Mar. Res.*, **50**, 367–384, https://doi.org/10.1357/002224092784797593.

Sasaki, H., P. Klein, B. Qiu, and Y. Sasai, 2014: Impact of oceanic-scale interactions on the seasonal modulation of ocean dynamics by the atmosphere. *Nat. Commun.*, **5**, 5636, https://doi.org/10.1038/ncomms6636.

Schubert, R., J. Gula, R. J. Greatbatch, B. Baschek, and A. Biastoch, 2020: The submesoscale kinetic energy cascade: Mesoscale absorption of submesoscale mixed layer eddies and frontal downscale fluxes. *J. Phys. Oceanogr.*, **50**, 2573–2589, https://doi.org/10.1175/JPO-D-19-0311.1.

Scott, R. B., and B. K. Arbic, 2007: Spectral energy fluxes in geostrophic turbulence: Implications for ocean energetics. *J. Phys. Oceanogr.*, **37**, 673–688, https://doi.org/10.1175/JPO3027.1.

Smith, K. S., 2007: Eddy amplitudes in baroclinic turbulence driven by nonzonal mean flow: Shear dispersion of potential vorticity. *J. Phys. Oceanogr.*, **37**, 1037–1050, https://doi.org/10.1175/JPO3030.1.

——, and G. K. Vallis, 2001: The scales and equilibration of midocean eddies: Freely evolving flow. *J. Phys. Oceanogr.*, **31**, 554–571, https://doi.org/10.1175/1520-0485(2001)031<0554:TSAEOM>2.0.CO;2.

——, and J. Vanneste, 2013: A surface-aware projection basis for quasigeostrophic flow. *J. Phys. Oceanogr.*, **43**, 548–562, https://doi.org/10.1175/JPO-D-12-0107.1.

Stanley, Z., S. D. Bachman, and I. Grooms, 2020: Vertical structure of ocean mesoscale eddies with implications for parameterizations of tracer transport. *J. Adv. Model. Earth Syst.*, **12**, e2020MS002151, https://doi.org/10.1029/2020MS002151.

Stone, P. H., 1972: A simplified radiative-dynamical model for the static stability of rotating atmospheres. *J. Atmos. Sci.*, **29**, 405–418, https://doi.org/10.1175/1520-0469(1972)029<0405:ASRDMF>2.0.CO;2.

Storer, B. A., M. Buzzicotti, H. Khatri, S. M. Griffies, and H. Aluie, 2022: Global energy spectrum of the general oceanic circulation. *Nat. Commun.*, **13**, 5314, https://doi.org/10.1038/s41467-022-33031-3.

Tailleux, R., and J. C. McWilliams, 2001: The effect of bottom pressure decoupling on the speed of extratropical, baroclinic Rossby waves. *J. Phys. Oceanogr.*, **31**, 1461–1476, https://doi.org/10.1175/1520-0485(2001)031<1461:TEOBPD>2.0.CO;2.

Talley, L. D., 1988: Potential vorticity distribution in the North Pacific. *J. Phys. Oceanogr.*, **18**, 89–106, https://doi.org/10.1175/1520-0485(1988)018<0089:PVDITN>2.0.CO;2.

Thompson, A. F., and W. R. Young, 2006: Scaling baroclinic eddy fluxes: Vortices and energy balance. *J. Phys. Oceanogr.*, **36**, 720–738, https://doi.org/10.1175/JPO2874.1.

Tulloch, R., J. Marshall, and K. S. Smith, 2009: Interpretation of the propagation of surface altimetric observations in terms of planetary waves and geostrophic turbulence. *J. Geophys. Res.*, **114**, C02005, https://doi.org/10.1029/2008JC005055.

——, ——, C. Hill, and K. S. Smith, 2011: Scales, growth rates, and spectral fluxes of baroclinic instability in the ocean.

J. Phys. Oceanogr., **41**, 1057–1076, https://doi.org/10.1175/2011JPO4404.1.

Vallis, G. K., 2017: *Atmospheric and Oceanic Fluid Dynamics*. Cambridge University Press, 946 pp.

Visbeck, M., J. Marshall, T. Haine, and M. Spall, 1997: Specification of eddy transfer coefficients in coarse-resolution ocean circulation models. *J. Phys. Oceanogr.*, **27**, 381–402, https://doi.org/10.1175/1520-0485(1997)027<0381:SOETCI>2.0.CO;2.

Wang, J., G. R. Flierl, J. H. LaCasce, J. L. McClean, and A. Mahadevan, 2013: Reconstructing the ocean's interior from surface data. *J. Phys. Oceanogr.*, **43**, 1611–1626, https://doi.org/10.1175/JPO-D-12-0204.1.

Wolfe, C. L., and P. Cessi, 2010: What sets the strength of the middepth stratification and overturning circulation in eddying ocean models? *J. Phys. Oceanogr.*, **40**, 1520–1538, https://doi.org/10.1175/2010JPO4393.1.

Wortham, C., and C. Wunsch, 2014: A multidimensional spectral description of ocean variability. *J. Phys. Oceanogr.*, **44**, 944–966, https://doi.org/10.1175/JPO-D-13-0113.1.

Wunsch, C., 1997: The vertical partition of oceanic horizontal kinetic energy. *J. Phys. Oceanogr.*, **27**, 1770–1794, https://doi.org/10.1175/1520-0485(1997)027<1770:TVPOOH>2.0.CO;2.

Yankovsky, E., L. Zanna, and K. S. Smith, 2022: Influences of mesoscale ocean eddies on flow vertical structure in a resolution-based model hierarchy. *J. Adv. Model. Earth Syst.*, **14**, e2022MS003203, https://doi.org/10.1029/2022MS003203.

Yassin, H., and S. M. Griffies, 2022a: On the discrete normal modes of quasigeostrophic theory. *J. Phys. Oceanogr.*, **52**, 243–259, https://doi.org/10.1175/JPO-D-21-0199.1.

——, and ——, 2022b: Surface quasigeostrophic turbulence in variable stratification. *J. Phys. Oceanogr.*, **52**, 2995–3013, https://doi.org/10.1175/JPO-D-22-0040.1.

Zhang, W., and C. L. P. Wolfe, 2022: On the vertical structure of oceanic mesoscale tracer diffusivities. *J. Adv. Model. Earth Syst.*, **14**, e2021MS002891, https://doi.org/10.1029/2021MS002891.

Zhang, X., Z. Jing, and P. Yang, 2023: Seasonality of upper-ocean vertical eddy buoyancy flux in the Kuroshio Extension. *J. Phys. Oceanogr.*, **53**, 1577–1590, https://doi.org/10.1175/JPO-D-22-0173.1.

Zhang, Z., Y. Zhang, W. Wang, and R. Huang, 2013: Universal structure of mesoscale eddies in the ocean. *Geophys. Res. Lett.*, **40**, 3677–3681, https://doi.org/10.1002/grl.50736.

——, ——, and ——, 2017: Three-compartment structure of subsurface-intensified mesoscale eddies in the ocean. *J. Geophys. Res. Oceans*, **122**, 1653–1664, https://doi.org/10.1002/2016JC012376.